

PL-TR-97-2013

**THEORETICAL, DIAGNOSTIC AND
EMPIRICAL IONOSPHERIC MODEL
DEVELOPMENT AND WAVE SIGNATURES
IN UPPER ATMOSPHERE DENSITY**

**Matthew W. Fox
Xiaoqing Pi
Jules Aarons
Jeffrey M. Forbes**

**Boston University
Center for Space Physics
725 Commonwealth Avenue
Boston, MA 02215**

January 1997

**Final Report
1 May 1993-31 December 1996**

19970603 124

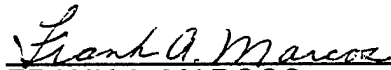
APPROVED FOR PUBLIC RELEASE; DISTRIBUTION UNLIMITED


DTIC QUALITY INSPECTED 3



**PHILLIPS LABORATORY
Directorate of Geophysics
AIR FORCE MATERIEL COMMAND
HANSCOM AFB, MA 01731-3010**

"This technical report has been reviewed and is approved for publication"


FRANK A. MARCOS
Contract Manager


EDWARD J. WEBER
Branch Chief


DAVID A. HARDY
Division Director

This document has been reviewed by the ESC Public Affairs Office (PA) and is releasable to the National Technical Information Service (NTIS).

Qualified requestors may obtain additional copies from the Defense Technical Information Center (DTIC). All others should apply to the National Technical Information Service (NTIS).

If your address has changed, or if you wish to be removed from the mailing list, or if the addressee is no longer employed by your organization, please notify PL/TSI, 29 Randolph Road, Hanscom AFB, MA 01731-3010. This will assist us in maintaining a current mailing list.

Do not return copies of this report unless contractual obligations or notices on a specific document requires that it be returned.

REPORT DOCUMENTATION PAGE			Form Approved OMB No. 0704-0188	
<small>Public reporting burden for this collection of information is estimated to average 1 hour per response, including the time for reviewing instructions, searching existing data sources, gathering and maintaining the data needed, and completing and reviewing the collection of information. Send comments regarding this burden estimate or any other aspect of this collection of information, including suggestions for reducing this burden, to Washington Headquarters Services, Directorate for Information Operations and Reports, 1215 Jefferson Davis Highway, Suite 1204, Arlington, VA 22202-4302, and to the Office of Management and Budget, Paperwork Reduction Project (0704-0188), Washington, DC 20503.</small>				
1. AGENCY USE ONLY (Leave blank)		2. REPORT DATE January 1997		3. REPORT TYPE AND DATES COVERED FINAL REPORT May 1 1993 - December 31 1996
4. TITLE AND SUBTITLE Theoretical, Diagnostic and Empirical Ionospheric Model Development, and Wave Signatures in Upper Atmosphere Density			5. FUNDING NUMBERS PE 63707F PR 4026 TA GL WU MA Contravt F19628-93-K-0012	
6. AUTHOR(S) Matthew W. Fox, Xiaoqing Pi, Jules Aarons and Jeffrey M. Forbes				
7. PERFORMING ORGANIZATION NAME(S) AND ADDRESS(ES) Boston University Center for Space Physics 725 Commonwealth Avenue Boston, MA 02215			8. PERFORMING ORGANIZATION REPORT NUMBER	
9. SPONSORING/MONITORING AGENCY NAME(S) AND ADDRESS(ES) Phillips Laboratory 29 Randolph Road Hanscom AFB, MA 01731-3010 Contract Manager: Frank Marcos/GPIM			10. SPONSORING/MONITORING AGENCY REPORT NUMBER PL-TR-97-2013	
11. SUPPLEMENTARY NOTES				
12a. DISTRIBUTION / AVAILABILITY STATEMENT Approved for public release; Distribution unlimited			12b. DISTRIBUTION CODE	
13. ABSTRACT (Maximum 200 words) To provide a better description of the ionospheric environment studies have been undertaken ranging from the expansion of scope of a theoretical ionospheric model, event modeling studies, and studies of new applications-oriented empirical models. The Phillips Laboratory Global Theoretical Ionospheric Model has been rewritten to solve for multiple ion densities, and physical drivers have been updated. A theoretical model has been used to study latitudinal symmetry in equatorial electron densities related to scintillation, ionospheric responses to substorms, the role of neutral winds at night, and the means by which F-region parameters may be derived from satellite in situ measurements. A model has been applied to the study of disturbed ionospheric conditions. Finally, on the applications side, studies were conducted showing that a new simple profile model has powerful ray-tracing applications and can be used to combine satellite measurements into full profiles. GPS satellites offer an opportunity for monitoring scintillations. Finally, SETA density measurements have been extensively utilized to both investigate and subsequently describe a series of wavelike and disturbed-conditions phenomena.				
14. SUBJECT TERMS Theoretical Ionospheric Modeling, Empirical Modeling, Scintillation Morphology, Neutral Density Wave Signature			15. NUMBER OF PAGES 64	
			16. PRICE CODE	
17. SECURITY CLASSIFICATION OF REPORT Unclassified	18. SECURITY CLASSIFICATION OF THIS PAGE Unclassified	19. SECURITY CLASSIFICATION OF ABSTRACT Unclassified	20. LIMITATION OF ABSTRACT SAR	

TABLE OF CONTENTS

1. INTRODUCTION	1
2. EXTENDING THE GTIM TO THE PLASMASPHERE	2
2.1 Deriving Ion Densities	2
2.2 Revising Model Drivers	5
2.3 Testing Model Stability and Reliability	7
3. MODELING STUDIES USING THE GTIM	10
3.1 The Equatorial Anomaly-Irregularities	10
3.2 Substorms	17
3.3 The Nighttime Ionosphere	18
3.4 Satellite Signatures	19
4. MODELING APPLICATIONS OF THE GTIM	22
4.1 Modeling Impulsive Disturbances	22
4.2 Modeling Wavelike Perturbations	24
5. APPLICATIONS STUDIES	27
5.1 Ionospheric Ray-Tracing	27
5.2 Sensing the F-Region From DMSP	30
5.3 Scintillations	31
6. MERIDIONAL WAVE STRUCTURES	33
6.1 Summary of Results	33
6.2 Method of Spectral Analysis	34
6.3 Periodogram Averaging	35
6.4 Wavelength Contribution to Signal Energy	36
7. MAGNETIC STORM PERTURBATIONS	39
7.1 Summary of Results	40
7.2 Sample Result	41
8. LONGITUDINAL WAVE STRUCTURES	46
8.1 Longitudinal/UT Variation	46
8.2 Longitudinal Wave Structures	53
REFERENCES	57

Illustrations

Figure 1. Electron (dot-dashed line) and ion densities (H^+ dotted, He^+ dashed, O^+ too small to be seen) at the apex of the L=3 fieldline for equinox, solar moderate conditions plotted as functions of the logarithm of density of artificially added neutral species, demonstrating reasonable insensitivity to that parameter. Panels side-by-side show the same results for different methods of linearizing the equation of continuity. Rows of panels correspond to results for 0200LT, 1000LT and 2200LT respectively, read from the top. 8

Figure 2. As in Figure 1, but for densities at the apex of L=3.8. 9

Figure 3. A comparison of modeled GTIM O^+ densities with observed profiles from the Arecibo, Puerto Rico, ISR. The four panels show comparisons at 1900LT, 2200LT, 0100LT and 0400LT. Observations are indicated by 25 April 1995 as solid lines, 26 April as dotted lines and 27 April as dashed lines. Overplots show radar observations made within 15 minutes. Symbols denote model densities for a 4-day simulation (day 1=plus, day 2=asterisk, day 3=diamond, day 4=triangle). 11

Figure 4. As in Figure 3, but pertaining to H^+ densities. The additional symbols, "G" demonstrate the results of the Gallagher empirical plasmaspheric model. 12

Figure 5. As in Figure 3, but pertaining to He^+ densities. 13

Figure 6. The two panels refer to the seasonal variations of Nmax at 1900 and 2100LT respectively. Each panel shows plots of Nmax at selected latitudes as a function of month during the year at the US sector. While the results at $\pm 10^\circ$ (dotted and dashed lines) are typically very similar, those at $\pm 20^\circ$ have been as a measure of the asymmetry, with the hand-drawn insert used to reflect the level of symmetry. 15

Figure 7. As in Figure 6, but for the Pacific sector. 16

Figure 8. GTIM results for Nmax and Hmax plotted against Millstone Hill radar measurements. The model has been run with both climatological neutral winds and with measured winds. The model run with adjusted winds show significant improvement in Hmax at night. The enhanced equatorward winds were able to maintain the nighttime ionosphere (Nmax) under active magnetic conditions. 20

Figure 9. Time variations of modeled Nmax values before and after the onset of a magnetic disturbance, at five selected latitudes. Leftmost in each plot is the quiet-time variations, and this is repeated as a dashed line for the subsequent days. The solid line shows the variation in Nmax following storm onset, and positive and negative storm phases being clearly apparent. 23

Figure 10. Wavelike ionospheric effects in the GTIM when a wavelike $\mathbf{E} \times \mathbf{B}$ disturbance is applied. This case was made for January, solar maximum, Huancayo sector conditions, using a 16-day wave and 50% peak-to-peak amplitude. The relative variation in Nmax at selected latitudes (18=solid line, -10=dotted, 0=dashed, +10=dot-dashed, +18=dot-dot-dot-dashed) is plotted as a function of the day during the period. 26

Figure 11. A demonstration of the abilities of the SIMPLI profile model in radiowave propagation predictions. Here, the solid line indicates the elevation angle versus transmission frequency for a given circuit obtained from climatological estimates (electron density contours in the left insert). The dotted line shows the same predictions made from the "ground-truth" ionosphere, shown in the right insert. The three topmost lines show the results when Nmax is updated at the circuit mid-point, end-points, and both, and when SIMPLI parameters along the path are shifted only the zeroeth order. The three lines lying nearest to the dotted line correspond to Nmax being refit along the whole path. 29

Figure 12. Averaged periodogram for quiet vs. active orbits in 1983. 37

Figure 13. Day vs. night averaged periodogram for 1983.	38
Figure 14. Kp variations for the July , 1983, and August, 1983 study periods.	42
Figure 15. Daytime density variations during July 20-27, 1983.	43
Figure 16. Same as Figure 15, except for nighttime.	44
Figure 17. Same as Figure 15, except for August, 1983 study period.	45
Figure 18. Comparison of SETA and MSISE90 density variations averaged over 20-20 degrees latitude at 1030 LT during July 20-26, 1983.	47
Figure 19. Comparison of "longitude/UT" variation in SETA densities (circles) with MSISE90 (dotted line) during the magnetically quiet period of July 21-23, 1983. Solid line represents least-squares fit of sinusoid to SETA data.	49
Figure 20. Comparison of amplitudes of "longitude/UT" variation between SETA and MSISE90 as a function of latitude, for daytime data during July 21-23, 1983.	50
Figure 21. Longitude/UT dependence as revealed by SETA (top) and MSISE90 (bottom) total mass densities at 200 km during July 21-23, 1983. Left: daytime (≈ 1030 LT). Right: nighttime (≈ 2230 LT).	51
Figure 22. Longitude/UT dependence as revealed in SETA (left) and MSISE90 (right) daytime (≈ 1030 LT) total mass densities at 200 km during December 5-10, 1983.	52
Figure 23. Density residuals as a function of latitude and time during magnetically quiet periods during July, 1983, and December, 1983.	55
Figure 24. Superposition of spectra in different latitude bands, corresponding to the density residuals depicted in Figure 17 for July, 1983.	56

1 Introduction

In order to provide a better description of the ionospheric environment a variety of studies have been undertaken covering a range of different approaches. These span the spectrum from the expansion of scope of a theoretical ionospheric model, passing through a series of event-oriented modeling studies, to the investigation of new applications-oriented empirical descriptions of ionospheric behavior.

From the empirically-based applications studies, new quick methods can be provided to users of real-time and monitoring systems to enhance their performance and capabilities, and new clues to underlying physical processes may be gleaned. From the event-oriented modeling studies, the validity of physical interpretation of particular ionospheric phenomena can be determined. From the expansion of a theoretical model to multiple ions and much greater altitudes, the scope of investigations are greatly enhanced and a new generation of specification model can ultimately be provided to the user.

The Phillips Laboratory Global Theoretical Ionospheric Model (hereafter, GTIM) has been rewritten to solve for multiple ion densities, and physical drivers have been updated. The GTIM has been utilized to demonstrate (1) that latitudinal symmetry in equatorial electron densities can be related to scintillation occurrence rates (2) that ionospheric responses to substorms can be investigated, (3) that neutral winds can play an important role in nighttime maintenance and (4) that satellite in situ measurements can be used to derive F-region parameters. The model has further been adapted to the study of disturbed ionospheric conditions, both of impulsive and periodic types. Finally, on the applications side, studies were conducted showing (1) that a new simple profile model has powerful ray-tracing applications, (2) that the same model can be used to combine satellite measurements from different sources and (3) that GPS satellites offer an opportunity for monitoring scintillations.

On the thermospheric side, Satellite Electrostatic Triaxial Accelerometer Experiment (hereafter SETA) density measurements have been extensively utilized to both investigate and subsequently describe a series of phenomena (1) meridional wave structures, (2) magnetic storm response and (3) longitudinal wave structures.

2 Extending the GTIM to the Plasmasphere

One significant effort over this period has been the extension of the Phillips Laboratory GTIM to the solution of multiple ion species over a significantly greater range of altitudes. This has involved two major areas of development within the model that were performed at Boston University:

- rewriting the equations of continuity and momentum for more than one ion, including both ion-ion and ion-electron interactions

- updating physical drivers for the model to permit reliable ion density derivations at much higher altitudes.

There has also been a significant effort made in validating the model results and in verifying the numerical stability of the ion densities. The multiple-ion GTIM, as described briefly in the following section, is considered to be reliable up to $L=3$.

Working code, and revised model drivers have been delivered to colleagues at Computational Physics Inc., in Boston. The multiple ion model was described in a presentation at the 1996 AGU Meeting, in San Francisco, CA, and is currently in preparation as a journal article.

2.1 Deriving Ion Densities

The GTIM solution method for a one-ion formulation is described in Anderson (1973). Essentially, an expression for ion flux derived from the momentum equation is substituted into the continuity equation. This expanded continuity equation is then finite-differenced,

and the resulting equation that is tridiagonal in the ion densities (denoted N_i), is solved numerically along magnetic field lines from the footpoint at 125km in one hemisphere to the conjugate point in the other hemisphere.

We now consider the multiple ion situation. In the first instance, we form an equivalent expression for ion fluxes from the momentum equation for each of a number of ions. The momentum equations include terms from each of collisions with other ions (say, j) and with electrons. The electron momentum equation is used to eliminate the electric field term in the manner of the one-ion formulation, and the resultant expression for ion fluxes is of the same general form as that obtained for one ion, permitting the same substitution into the continuity equation and the same type of numerical solution. However, in three ways, the expression is more complex than the one-ion case:

- ion density and electron density are no longer equal, and N_i/N_e terms appear in the expression
- ion-ion interactions are included, and ion velocities become important to the solution as the relative velocities between ions define the momentum transfer
- ion-ion couplings for the i th ion also include coupling of the j th ion with electrons, owing to the electric field term in the momentum equation.

Thus, strictly speaking, the equation for ion flux is not linear in N_i . On the other hand, the higher order terms are generally small and can be arranged to appear only as modifiers to collision frequencies. Rearranging the higher order terms and determining these effective collision frequencies are key steps in obtaining density solutions in the multiple ion GTIM.

We have thus outlined an approach for deriving ion densities for each of a number of different species. The ions required to define the ionosphere and plasmasphere are O^+ , H^+ and He^+ , and solutions are sought for each ion in turn at each time step. Because the ion

densities are solved sequentially rather than simultaneously, much care is taken to ensure that ions are not artificially created or destroyed as numerical artifacts in any time step. This involves making adjustments to both production and loss rates and is best illustrated in an example.

Let us look at the $O^+ - H^+$ charge exchange reaction and first consider the situation at an altitude of around 300km. The loss rate (β) for O^+ due to this charge exchange amounts to typically 30% of the total O^+ loss rate, and thus, when this reaction is included in the calculations, model F-region O^+ densities drop by around 30%. However, at these low altitudes, no H^+ can be formed, owing to the rapid loss of H^+ through the reverse reaction. In this situation, the answer is to modify the forward loss rate by a factor that depends on the reverse loss rate (β_{REV}) and the time step (ΔT). We say that the fraction of O^+ that can be lost out of the amount one is trying to lose is the same as the fraction of H^+ that one is able to form over the time step, and that the rest charge exchanges rapidly back to O^+ . Specifically, this fraction is $\exp(-\beta_{REV}\Delta T)$.

At a higher altitude (say, 1500km), $O^+ - H^+$ is primarily a source of O^+ . One derives a production term (locally) for O^+ that goes as $\kappa n(H^+) n(O) \Delta T$. However, this production should not physically exceed the density of the available source terms (here H^+ and O, mostly the latter being the smaller term at high altitudes). To ensure this, production rates are modified by a factor of $\exp(-\kappa n(H^+) \Delta T)$ to reflect the fraction of O that can be lost over the time step. It should also be noted that because both $n(O)$ and $\beta_{REV}(H^+)$ are steeply varying functions of altitude, that the altitude profiles of these $\exp(-X \Delta T)$ terms are effectively step functions, and that the choice of how one averages these decay terms over the time step ($\exp(-X \Delta T)$ vs $\exp(-X \Delta T/2)$, say) has no influence on the final densities derived in the model.

2.2 Revising Model Drivers

As outlined above, each ion density can be derived from an expanded continuity equation (using effective ion fluxes), that becomes a tridiagonal matrix when finite-differenced. The coefficients that relate the adjacent terms in this matrix are dependent on a number of factors. Some of these factors are those that define the physical environment in which the ion density solutions are being derived, such as thermospheric densities and winds, electron and ion temperatures, and vertical $\mathbf{E} \times \mathbf{B}$ drifts. In the GTIM formulation, these physical quantities are not derived but are simply input, and are referred to as physical drivers for the (ionospheric) model.

Two important drivers have undergone recent revisions, specifically to address the issue of the higher altitudes being studied in the multiple ion GTIM.

First, vertical drifts have been generalized to include a variation with altitude. Most commonly this takes the form of using input values (based on Jicamarca or AE observations) at low altitudes, tapering off above one input altitude to zero by a second input altitude. An additional term in the continuity equation resulting from the non-zero dV/dZ has been included. Furthermore, because this term can influence ion densities at the 10% level, the altitude dependence has been made smooth in the first derivative to avoid discontinuities in densities with altitude (runs at adjacent L-shells). A tanh dependence is used. The input altitudes that define the vertical dependence were seen to vary with solar activity, and possibly other factors.

Next, the specification of electron and ion temperatures has been revised. Brace and Theis (1981) provided a convenient tabulation of a summary of measured T_e at several altitudes (300km, 400km, 1400km and 3000km). At each location in the GTIM, a system has been set up that provides a smooth fit with altitude to the Brace and Theis values at that location, using a tanh functional form. The fit is further constrained by the following

conditions:

- T_e is set to the neutral temperature (from MSIS) at the fieldline base altitude (125km)
- T_e being monotonic increasing with altitude at any location (not the same as monotonic increasing along the fieldline)
- T_e being smoothly and slowly varying (larger rates of change lead to anomalously high ion velocities in the model that in turn lead to large density gradients and sometimes numerical instabilities).

The second and third points mean that the fit will not necessarily pass through the Brace and Theis values, but will instead be a smooth fit guided by those values.

At higher altitudes than 3000km, it is not sufficient to simply set T_e to the 3000km value. In filling the plasmasphere, the model is basically diffusing light ions up both hemispheres of a fluxtube until the pressure gradient term balances the gravity term (in the momentum equation). A flat T_e profile above 3000km would mean that much larger light ion densities are required at high altitudes to achieve this balance, and that the model refilling time is very long (tens of days). Above 3000km, we have included a simple linear gradient in T_e with altitude, and to avoid ion velocity related instabilities in the solution from steep temperature gradients, there is an additional transition region above 3000km where the T_e gradient changes linearly with altitude from the 3000km value to the input asymptotic value at a higher altitude (say, 4000km). In this fashion, light ion densities converge within ten days or so, depending on altitude.

The ion temperature, T_i , is derived from T_e and T_N via a simple formulation of Banks and Kockarts (1973) that ensures a match with T_N at low ionization fraction, and T_e at higher altitudes/fractions.

2.3 Testing Model Stability and Reliability

A couple of important issues regarding model stability and reliability have been recently addressed.

The first issue arises from the higher order terms in N_i that appear in the multiple ion momentum equation for the i th ion. There are different methods of rearranging the higher order terms to make the expression apparently linear in N_i to facilitate the GTIM solution for densities in the expanded continuity equation. Thus, it is important to show that the derived densities do not depend on the method of rearranging used.

The second issue arises from the use of ion fluxes from the momentum equation in the continuity equation, as it relies on collisions between species to define those fluxes. At sufficiently high altitudes, collisions are too rare, and artificial neutral atoms are added to achieve numerical stability. Thus, it is important to chronicle when these additional neutrals are required, and when they start to influence the densities derived.

Figure 1 demonstrates results obtained for ion densities at the apex of the $L=3$ fieldline for equinox, solar moderate conditions for a five day run. Each panel shows densities of each ion (and electrons) at a particular local time as a function of the logarithm of density of neutrals added. Flat lines thus indicate the desired insensitivity of the results to this numerical artifact. Adjacent panels show the same results using different methods of treating higher order terms in N_i , and the overall consistency of ion densities (to 10% or so in this case) demonstrates insensitivity to the method. Other rows show the same behavior at other local times. The results are seen in Figure 1 to be encouraging at $L=3$. However, by $L=3.8$, as seen in Figure 2, the sensitivity to both neutrals and method is much more substantial (say, 50%), demonstrating that a different solution approach will be required at the highest altitudes in the plasmasphere.

At lower altitudes, reasonable agreement with observed ion densities has been

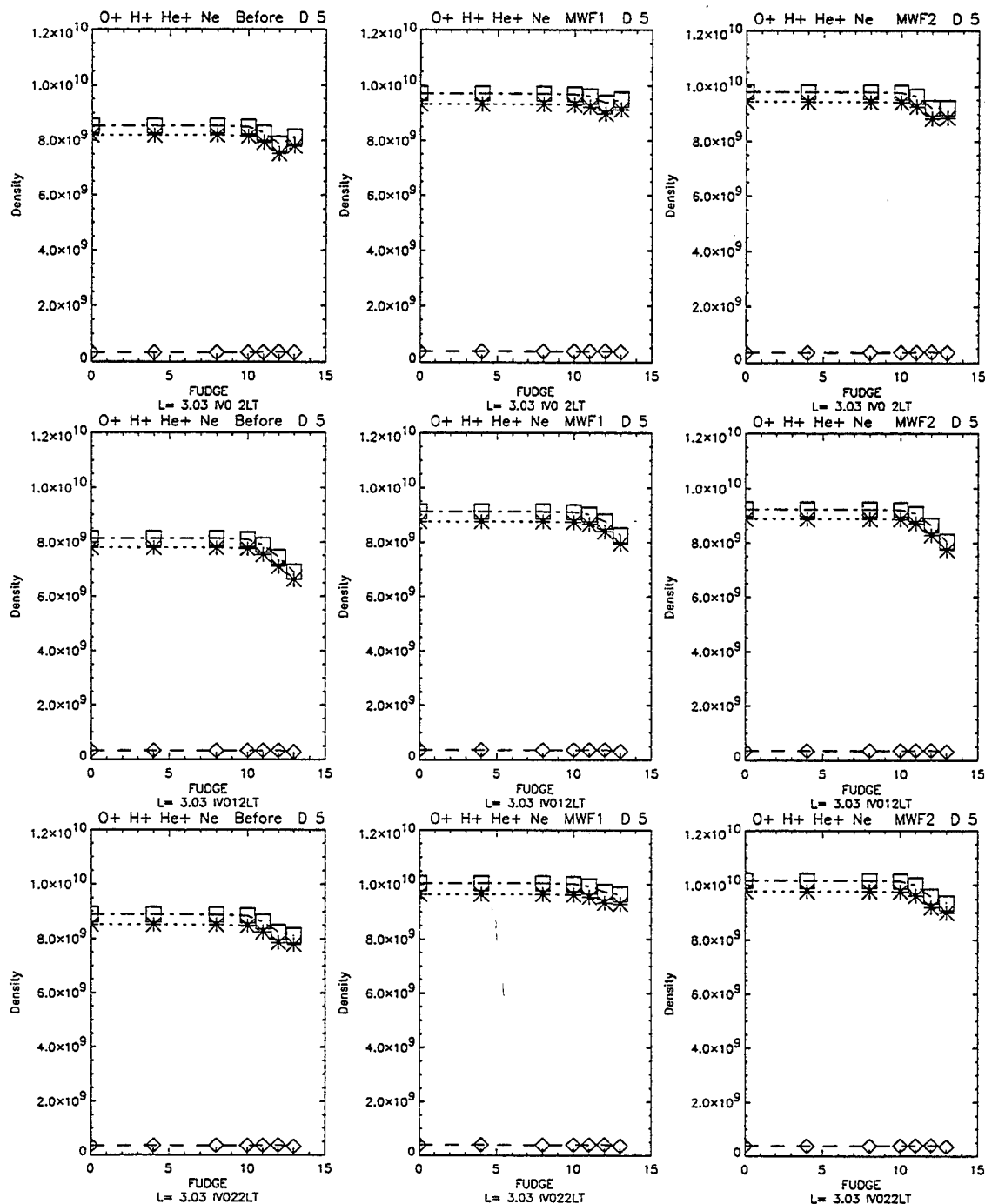


Figure 1. Electron (dot-dashed line) and ion densities (H^+ dotted, He^+ dashed, O^+ too small to be seen) at the apex of the $L=3$ fieldline for equinox, solar moderate conditions plotted as functions of the logarithm of density of artificially added neutral species, demonstrating reasonable insensitivity to that parameter. Panels side-by-side show the same results for different methods of linearizing the equation of continuity. Rows of panels correspond to results for 0200LT, 1000LT and 2200LT respectively, read from the top.

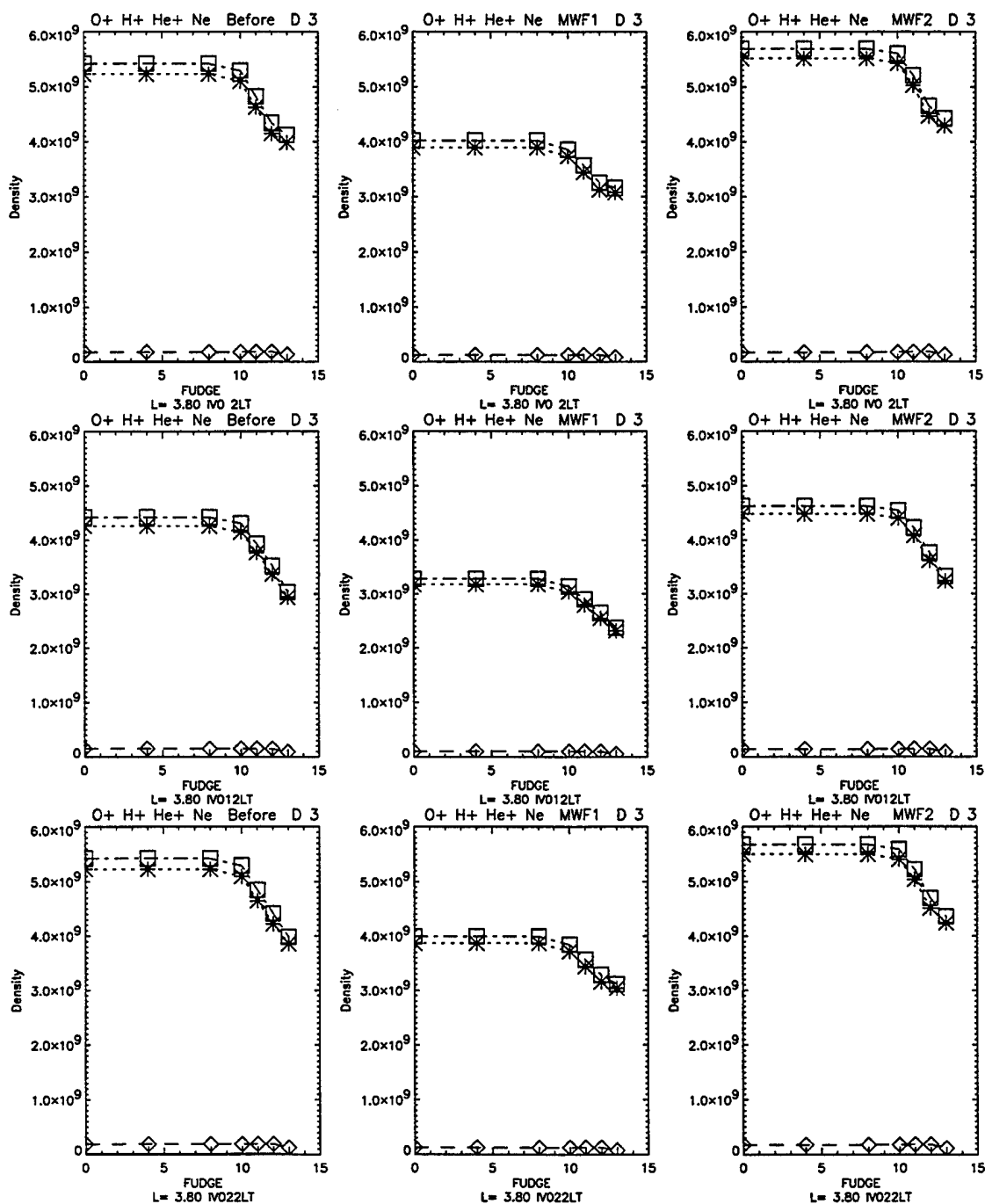


Figure 2. As in Figure 1, but for densities at the apex of L=3.8.

obtained. Figures 3, 4 and 5 show comparisons of modeled profiles of O^+ , H^+ and He^+ respectively, for selected local times and Arecibo ISR measured profiles from April 1995. In each panel, the different linestyles demonstrate the variations/uncertainties in the observations, while the symbols show the model results for consecutive run days. Overlapping symbols demonstrate convergence in the model densities, and qualitative and quantitative agreement with the observations is quite reasonable to 2000km. Comparisons have also been made with climatological DMSP in situ measurements, kindly made available by Dr. Fred Rich at Phillips Laboratory, and again the results are generally encouraging, especially for the major ion.

Overall, He^+ has not been seen in the model to ever be the major ion, but it is often evident in the 10-30% of total electron densities. H^+ - O^+ transition heights in the model are seen at altitudes as low as 500-600km, in line with many observations made at solar minimum.

3 Modeling Studies Using the GTIM

In terms of being able to perform diagnostic modeling studies, an advantage of the GTIM is that the thermospheric and electrodynamic environment of the ionosphere is input, rather than being derived in a self-consistent manner. It is thus straightforward to investigate the ionospheric effects of varying a variety of important physical drivers, many of which will not be known in an operational sense. Modeling studies of this type can thus help to isolate physical processes by their ionospheric signatures. Several such studies are described in the following section.

3.1 The Equatorial Anomaly-Irregularities

Ionospheric irregularities are a typical occurrence at equatorial latitudes, and the morphology of their behavior has been described observationally both in terms of season and longitude. A theoretical modeling study of these features in the equatorial anomaly

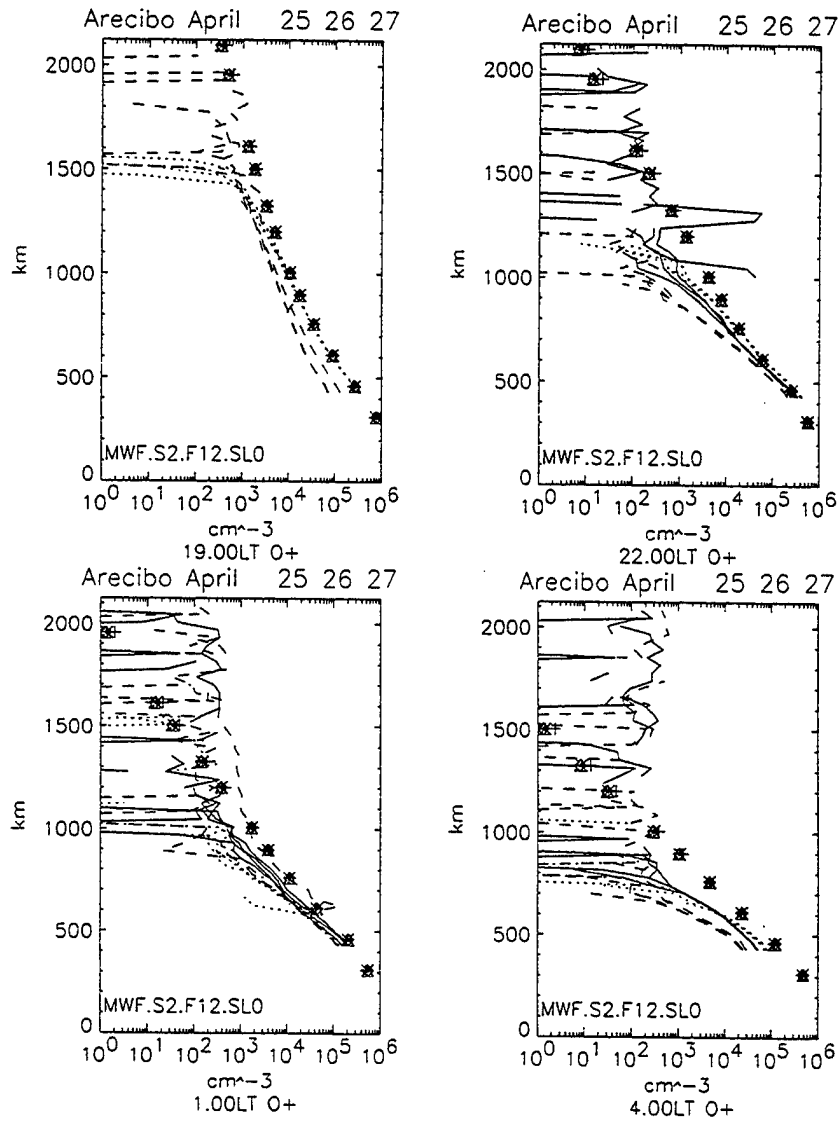


Figure 3. A comparison of modeled GTIM O^+ densities with observed profiles from the Arecibo, Puerto Rico, ISR. The four panels show comparisons at 1900LT, 2200LT, 0100LT and 0400LT. Observations are indicated by 25 April 1995 as solid lines, 26 April as dotted lines and 27 April as dashed lines. Overplots show radar observations made within 15 minutes. Symbols denote model densities for a 4-day simulation (day 1=plus, day 2=asterisk, day 3=diamond, day 4=triangle).

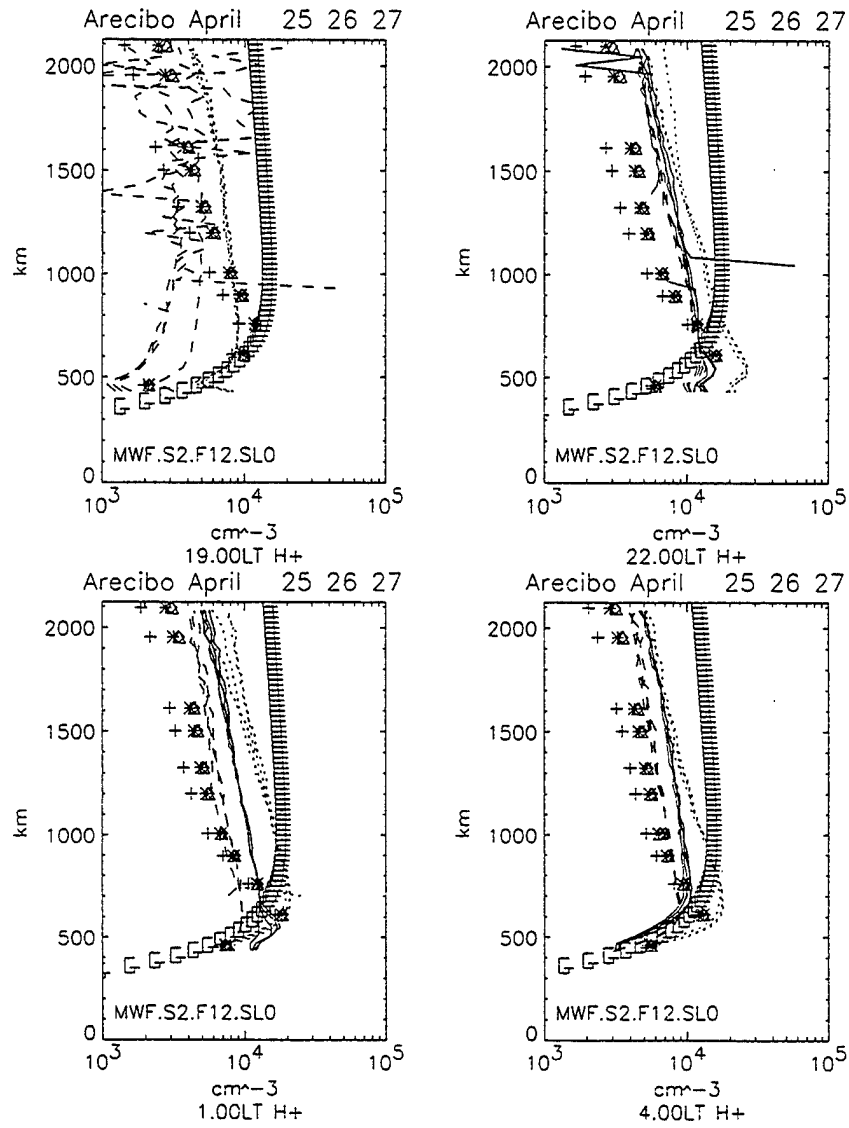


Figure 4. As in Figure 3, but pertaining to H^+ densities. The additional symbols, "G" demonstrate the results of the Gallagher empirical plasmaspheric model.

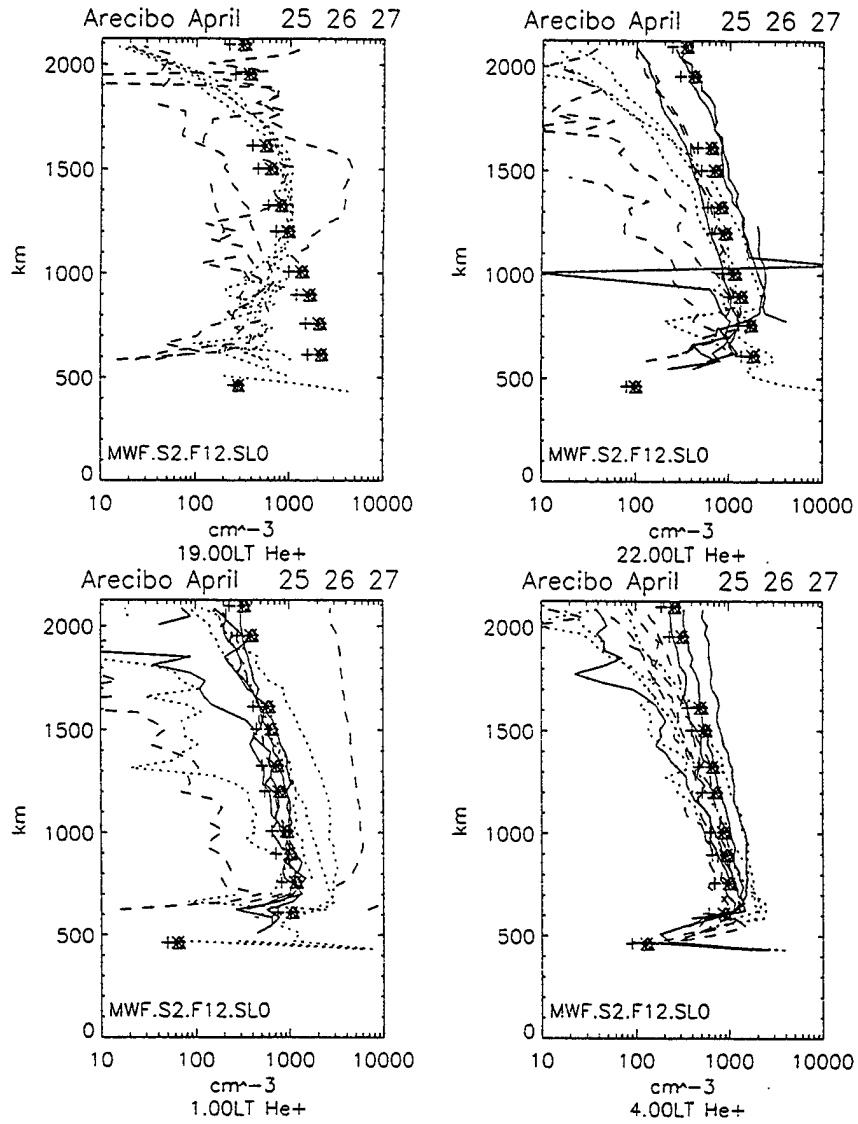


Figure 5. As in Figure 3, but pertaining to He^+ densities.

region was performed with a particular view to isolating disturbance effects. The GTIM is driven by three inputs that vary with geomagnetic activity. These are (1) the neutral atmosphere (from MSIS) (2) the neutral wind field (from the NASA model) and (3) the vertical $\mathbf{E} \times \mathbf{B}$ plasma drifts. It was next necessary to derive storm-time $\mathbf{E} \times \mathbf{B}$ drift patterns. Alterations were made to the drift patterns in three ways, that seemed to best summarize the changes in the drift patterns (1) at the pre-reversal enhancement (PRE) (2) towards the daytime peak (0900-1400LT) (3) towards the nighttime minimum (0000-0500LT).

Model runs were made to compare with a recent qualitative summary of the morphology of the occurrence of scintillation at low-latitude stations at four distinct longitude regions, characterized by the presence of stations and the magnetic declination. The results were examined with a view to quantifying the level of latitudinal symmetry in densities in the local ionosphere. Broadly speaking, the months at each location where the symmetry in Ne is highest match the months of highest spread-F occurrence (and thus scintillations). Here, we refer to Figures 6 and 7 to show the seasonal variations of density asymmetry in the model in the US and Pacific sectors, respectively. The two panels refer to results at 1900 and 2100LT respectively. Each panel shows plots of Nmax at selected latitudes as a function of month during the year at the named sector. While the results at $\pm 10^\circ$ (dotted and dashed lines) are typically very similar, those at $\pm 20^\circ$ have been as a measure of the asymmetry, with the hand-drawn insert used to reflect the level of symmetry. Referring to the descriptions of Aarons (1993), the US sector results resemble those seen in Huancayo, and those in the Pacific sector resemble Kwajalein, strongly peaked in equinox months.

While the mean thermospheric wind model of Hedin et al. (1988) is apparently sufficient to model the climatology of spread-F, as demonstrated above, case studies should

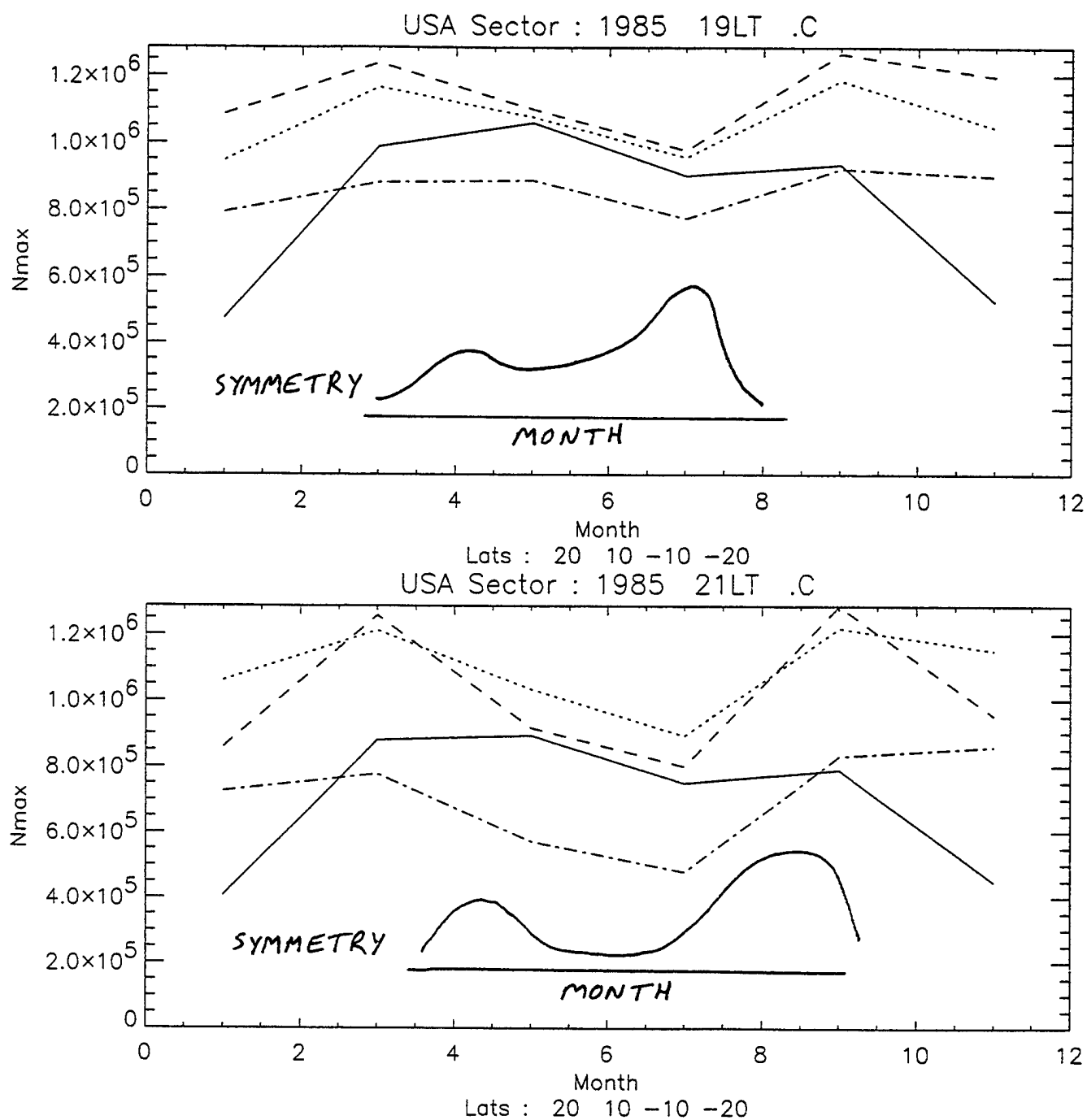


Figure 6. The two panels refer to the seasonal variations of N_{max} at 1900 and 2100LT respectively. Each panel shows plots of N_{max} at selected latitudes as a function of month during the year at the US sector. While the results at $\pm 10^\circ$ (dotted and dashed lines) are typically very similar, those at $\pm 20^\circ$ have been as a measure of the asymmetry, with the hand-drawn insert used to reflect the level of symmetry.

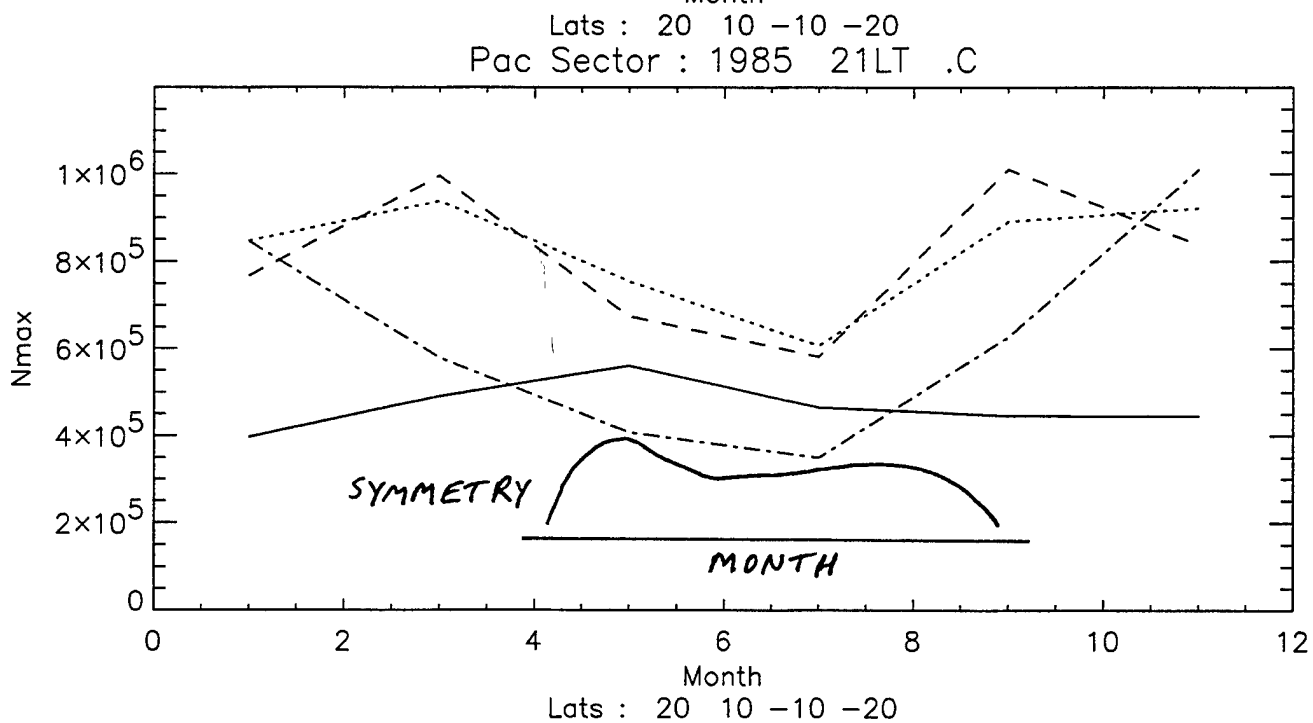
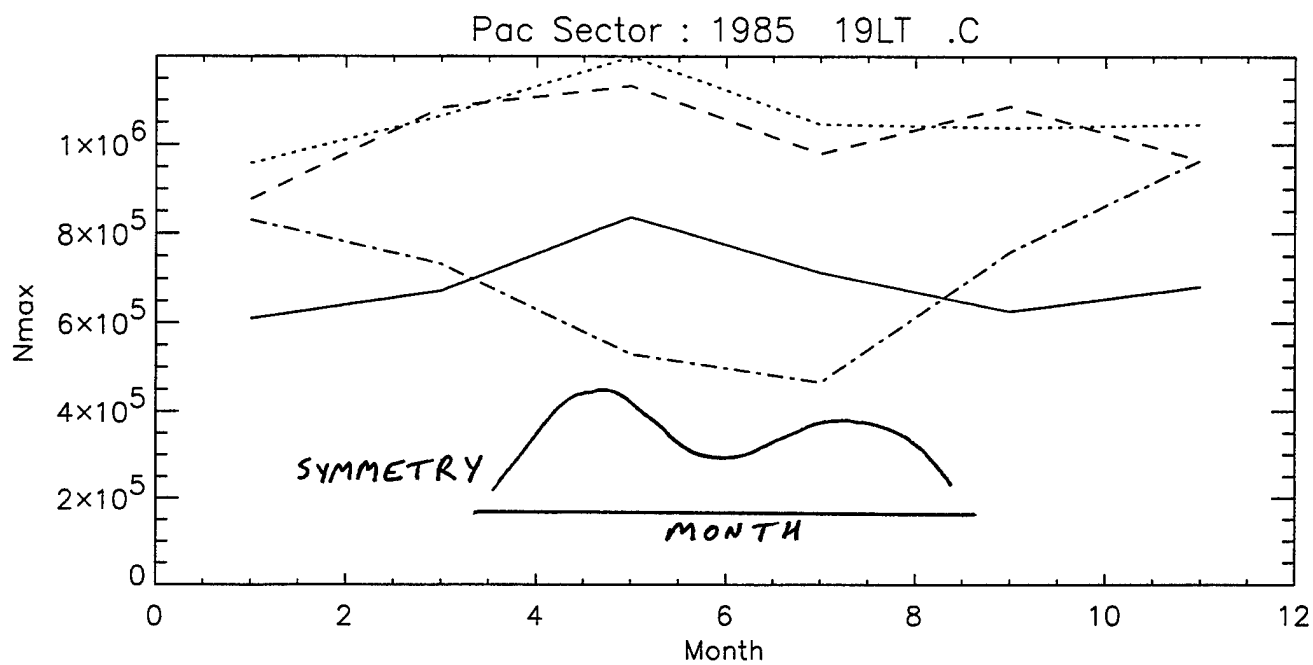


Figure 7. As in Figure 6, but for the Pacific sector.

be based upon measurements of neutral winds whenever these are available, given the role of winds in determining symmetry at low latitudes.

In the manner outlined above the same modeling study has been conducted including disturbance effects on the vertical drifts. Broadly speaking, the seasonal variations of symmetry in modeled electron density are different during disturbed periods. The prediction from these model runs is that the likelihood of scintillations during storms at these two longitude sectors will be less peaked at equinoxes, with occurrence at the June solstice becoming almost as likely as at equinoxes. This does not, however, factor in the higher occurrence rates of storms during equinox months.

3.2 Substorms

Here, the GTIM was used to simulate total electron content (TEC) disturbance events observed at middle and lower latitude sites near 75°W and 7°E longitudes during substorms. Within this longitudinal range, the daytime TEC disturbances show a pattern in which a positive response can be followed by a negative response or depletion, or diurnal double maxima (DDM) patterns if substorm activities are repeated. The required dayside electric fields in both longitudes showed eastward and westward perturbations during substorm expansion and subsidence phases, respectively. This is suggestive of magnetospheric electric field penetration and subsequent overshielding effects. The morphological features of the required electric field perturbations near dawn and dusk were examined to derive the local time characteristics of magnetospheric influence. Large scale traveling atmospheric disturbances (TADs) were also investigated in the model.

The ionospheric positive response to substorms has long been suggested to be due to TADs (historically travelling ionospheric disturbances, TIDs, referring to the ionospheric effects) in middle latitudes. There is a time delay of the ionospheric peak height behavior at middle latitudes relative to substorm activity shown at high latitudes, attributed to TAD

propagation. This raises the possibility of other dynamical sources which can rapidly affect the global ionosphere, such as electrodynamic effects. In addition, the TAD mechanism for producing observed TEC disturbances also needs to address the issue of TAD's appearing from the opposite hemisphere as substorms subside, as well as their long duration and very rapid propagation speeds.

We have identified a consistent daytime ionospheric disturbance pattern at middle and lower latitudes during substorms; namely, an ionospheric TEC positive response corresponding to substorm expansion periods, followed by a depletion or negative response as the substorm subsides. This work in this section was published as Pi et al. (1995).

3.3 The Nighttime Ionosphere

To investigate the issue of nighttime and topside maintenance of the ionosphere, the GTIM was run at middle latitudes and compared with incoherent scatter radar measurements. A request for an ionospheric experiment was made by Xiaoqing Pi and David N. Anderson to the Atmospheric Research Group, Haystack Observatory, to measure electron density profiles, meridional neutral winds, and electron fluxes under conditions of solar minimum, winter, and particularly at night. Such an experiment was conducted three times during December, 1994 and January, 1995, of about 24 hours duration each, using the Millstone Hill incoherent scatter radar (ISR) and the coordinated Fabry-Perot interferometer (FPI) operated by the Atmospheric Research Group. The calibrated radar data are accessible via internet at a web site (<http://hyperion.haystack.edu/homepage.html>, datafile=mil950130g.004).

The GTIM was run under both climatological and real conditions appropriate to January and April, 1995. The Kp index of January 30-31, 1995 show that geomagnetic conditions were active during the experiment. The model with standard input (MSIS and the NASA wind model) gave results that matched the daytime ionospheric electron density

profiles quite well, but underestimated the nighttime values. In the topside, the O^+ model underestimated the measurements above 600 km.

Some model input adjustments have been made to match the nighttime ionospheric measurements. One adjustment was to replace the model winds with the measured meridional neutral winds. The wind measurements were made using both ISR and FPI techniques, and two measurements showed much larger nighttime equatorward winds (300 m/s or more) than the model, though the two measurements differ to some extent. These strong nighttime equatorward winds may have been due to magnetic activity. The winds derived from the radar measurements have been taken for the model run due to its availability in both day and night. The model run with the wind adjustment gave good agreement in nighttime N_{max} , but showed higher N_{max} values than the daytime measurements. The model results with adjusted winds also showed significant improvement in H_{max} at night. This is seen in Figure 8, where the two panels compare N_{max} and H_{max} model results with the radar observations. These model runs indicated that the enhanced equatorward winds were able to maintain the nighttime ionosphere under active magnetic conditions at this subauroral site. Maintenance of higher densities in the topside may well be provided by H^+ ions and by charge exchange with O acting as a source for O^+ .

This work was presented at the 1995 CEDAR workshop in Boulder, CO.

3.4 Satellite Signatures

The goal of this project was to determine what may be deduced about the dayside ionosphere and the ambient neutral winds and vertical drifts given only an in situ electron density measurement, $Ne(840)$, in order to enhance the real-time ionospheric monitoring capabilities of the DMSP satellite system.

A modeling study was undertaken using the O^+ GTIM. Important inputs to the model are the specified diurnal variations of both the vertical ion drifts and the meridional

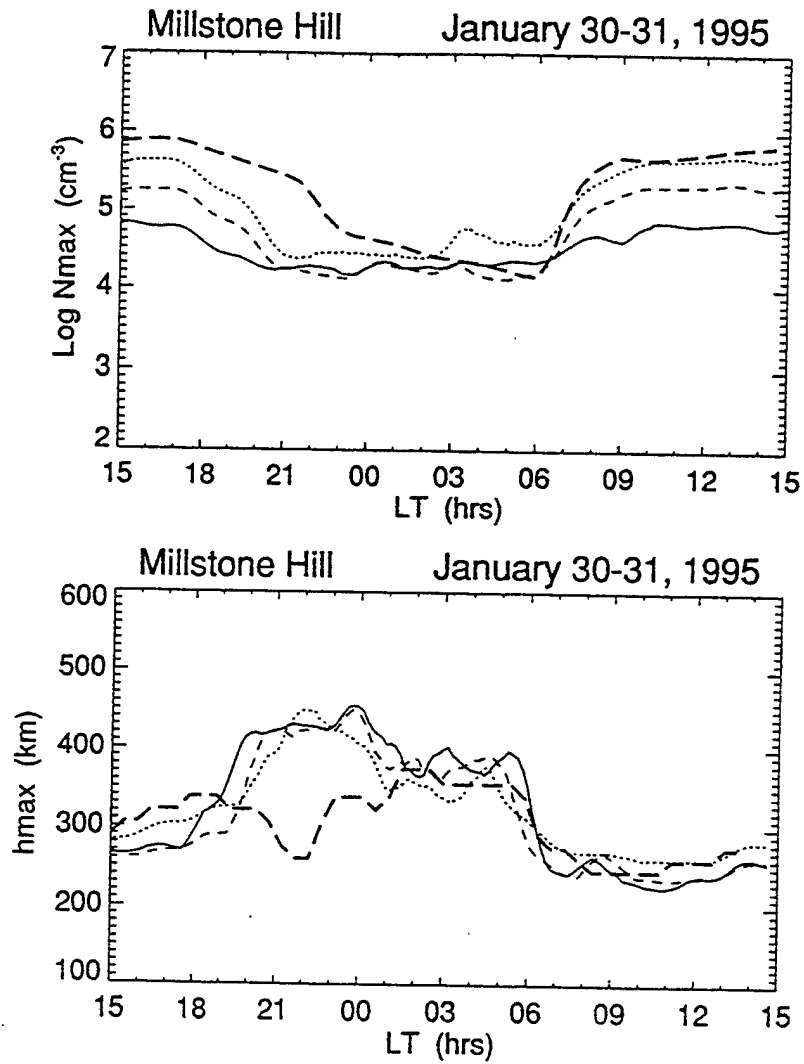


Figure 8. GTIM results for N_{max} and H_{max} plotted against Millstone Hill radar measurements. The model has been run with both climatological neutral winds and with measured winds. The model results with adjusted winds also show significant improvement in H_{max} at night. The enhanced equatorward winds were able to maintain the nighttime ionosphere (N_{max}) under active magnetic conditions at this subauroral site.

neutral wind. In an operational sense, there will be no additional information available on the ambient levels of drifts and winds, and thus, any proposed method must be made robust with respect to independent variations in both quantities. It became apparent that in many cases a single relationship between the desired ionospheric parameter existed for all levels of wind and drift, while in other cases separate relationships were defined for each wind or drift level. And in the latter case a separate means of estimating the wind or drift will be required. The procedure for establishing a set of algorithms for deriving N_{max} and H_{max} (and secondarily, effective wind and effective drift) was interactive, and was performed as follows:

- for a given season, level of solar activity, and local time, plot N_{max} (or H_{max}) as a function of $Ne(840)$ at a range of latitudes (each plot covering all wind and drift levels for one latitude)
- flag those latitudes where no knowledge of wind or drift level is required
- at other latitudes, determine whether separate relationships for either wind or drift level (a choice made from visual inspection)
- determine a latitude where an estimate of wind or drift can be made purely from the value of $Ne(840)$ (specifically, at higher latitudes, vertical drifts have little influence, and thus estimates of wind can be made- similarly at the equator, the vertical drifts dominate and thus, $Ne(840)$ usually provides a guide to the effective drift level).

Such a set of coefficients has been developed. An error analysis has shown that the standard deviation of the algorithms is around 5-20% in N_{max} , and slightly less in H_{max} . Ignoring outliers, the standard deviations are 5-10% in both N_{max} and H_{max} . The outliers arise from poor estimates made for effective wind or drift, and thus, it is preferable to base estimates of these quantities on $Ne(840)$ values from more than one latitude in each case (assuming that the wind or drift level applies to the whole region and not just locally, that

the variations are physically driven).

4 Modeling Applications of the GTIM

The GTIM determines a converged solution for the diurnal variation of O^+ density under conditions that are essentially repeating each day. Attempts have been made here to adapt the model for some level of real-time responsiveness, i.e., where conditions are changing from one time step to the next. Two studies of this type have been conducted.

4.1 Modeling Impulsive Disturbances

Initially, the model is run to achieve converged conditions for what is basically the quiescent ionosphere prior to the disturbance onset. At the desired onset time of the storm, a different set of A_p values are invoked to drive the neutral atmospheric wind and density models (these drive the effects at middle latitudes) and a different (perturbed) diurnal vertical drift pattern is used (driving the effects at low latitudes) along the lines described in Section 3 of this report. The perturbed winds and drifts are applied for a preset time, and the A_p history subsequently allows the model ionosphere to relax to the pre-onset conditions.

Some interesting results were obtained at low latitudes. For example, at latitudes -10, 0 and +10, a positive phase is predicted by the model in the evening sector for onset times early in the day. Slight negative phases are predicted at -20 and +20 degrees. However, when storm onset occurs later in the day, there is an evening negative phase predicted at -10 and +10, and a slight positive phase at -20 and +20. This latter point is shown in Figure 9, where the five rows show the variation of N_{max} with local time at the five named latitudes. Leftmost in each plot is the quiet-time variations, and this is repeated as a dashed line for the subsequent days. The solid line shows the variation in N_{max} following storm onset, and positive and negative storm phases being clearly apparent. Overall, the modeled

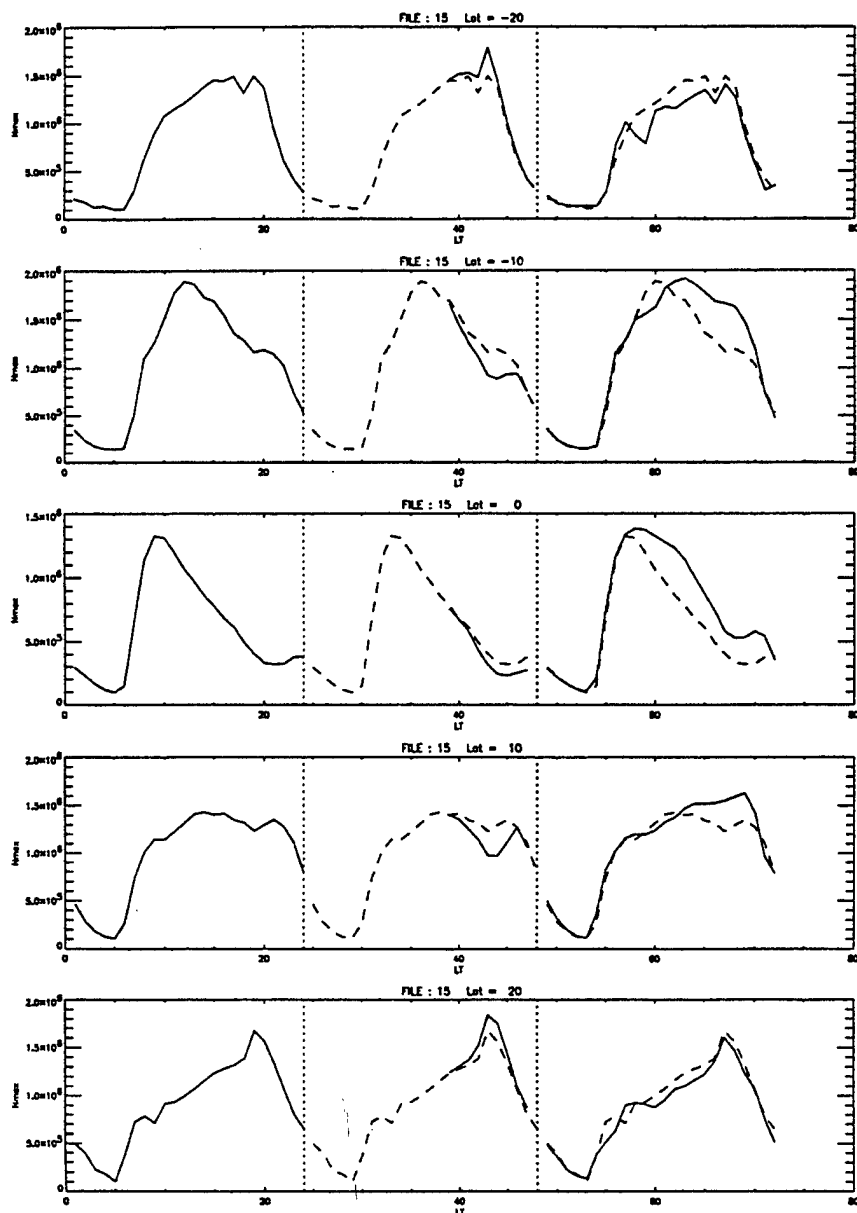


Figure 9. Time variations of modeled N_{max} values before and after the onset of a magnetic disturbance, at five selected latitudes. Leftmost in each plot is the quiet-time variations, and this is repeated as a dashed line for the subsequent days. The solid line shows the variation in N_{max} following storm onset, and positive and negative storm phases being clearly apparent.

ionospheric storm response depended both on the local time at onset and the latitude under consideration.

To drive the model for middle latitude case studies, initial conditions are first achieved by setting a constant A_p value of 3. At storm onset, the actual A_p history of the storm to be modeled is utilized, and also updated each three hours of the modeling run for subsequent days. At middle latitudes, it was shown that storm-related thermospheric changes can drive significant ionospheric response in the model. There is often a good level of agreement with observations of storm-time ionospheric parameters provided by the storm-driven GTIM. Consistently, the most difficult “features” to describe by the model are the rapid excursions that the climatological thermosphere will not follow, and those occurring in predawn hours (when the theoretical model is not always able to maintain the ionosphere, and the baseline description is not therefore as reliable). The storm response in the model is a fairly rapidly decreasing function of latitude. Overall, the level of broad agreement attained does strongly suggest that thermospheric influences are dominant in the middle latitude disturbed ionosphere, and that even the climatological model MSIS can provide a plausible foundation for this work.

4.2 Modeling Wavelike Perturbations

A version of the Phillips Laboratory GTIM has been developed that utilizes vertical drift fields with wavelike perturbations. As above, the model is first allowed to converge to quiescent conditions, before at a predetermined time the vertical drifts have a sinusoidal variation imposed upon them.

In its default configuration, the GTIM will terminate when an L-shell reaches a preset minimum value (around 1.026). This needs to be circumvented if one is to study waves of long periods on low altitude fieldlines. In essence, the method currently employed is one that keeps track of how far below this minimum value the L-shell is apparently drifting,

while keeping it at the minimum value until it drifts sufficiently upward to compensate (equivalently, there is a lower boundary set to the vertical dependence of vertical drifts, with a running measure taken for each fieldline to ensure that no net drift over a wave period is obtained). A figure of 5% is considered to be the reliability of the method (determined from numerical tests using a zero-amplitude wave) and only wave-related effects of greater than this are regarded as significant.

Subsequently, a series of model runs have been conducted appropriate to conditions where a 16-day periodicity was observed in ionospheric data (Forbes and Leveroni, 1992). Conditions were January, solar maximum (1979), US sector, and in the data some 20-30% (peak-peak) variations were seen in noontime Nmax. The series of model runs were based on several different onset-times for the wavelike variation in the vertical drift pattern, as well as for two different amplitudes, 10% and 25% (20% and 50% peak-peak). It was noted that for 16-day waves, the model results were not sensitive to the onset-time of the wave. Also, the amplitude of the ionospheric effects were not linearly related to the amplitude of the input disturbance.

Figure 10 shows one means of displaying the results. Here, the four panels show variations in Nmax as a function of day in the wave for selected local times (0600LT, 1200LT, 1800LT and 2400LT). Each panel shows the results for a number of different (magnetic) latitudes (-18=solid, -10=dotted, 0=dashed, 10=dot-dashed, 18=dot-dot-dot-dashed). This wave had a peak-peak amplitude of 50%, and an onset time of 1300LT.

The following points are noted, for this displayed case, and in general: (1) the corresponding ionospheric responses are largely wavelike, (2) effects are largest at midnight, (3) equatorial effects are opposite in phase to ΔE (equally, ΔH), (4) at local times where there is an anomaly crest, effects inside and outside the crests are opposite in sign and (5) effects in Hmax are much smaller than in Nmax.

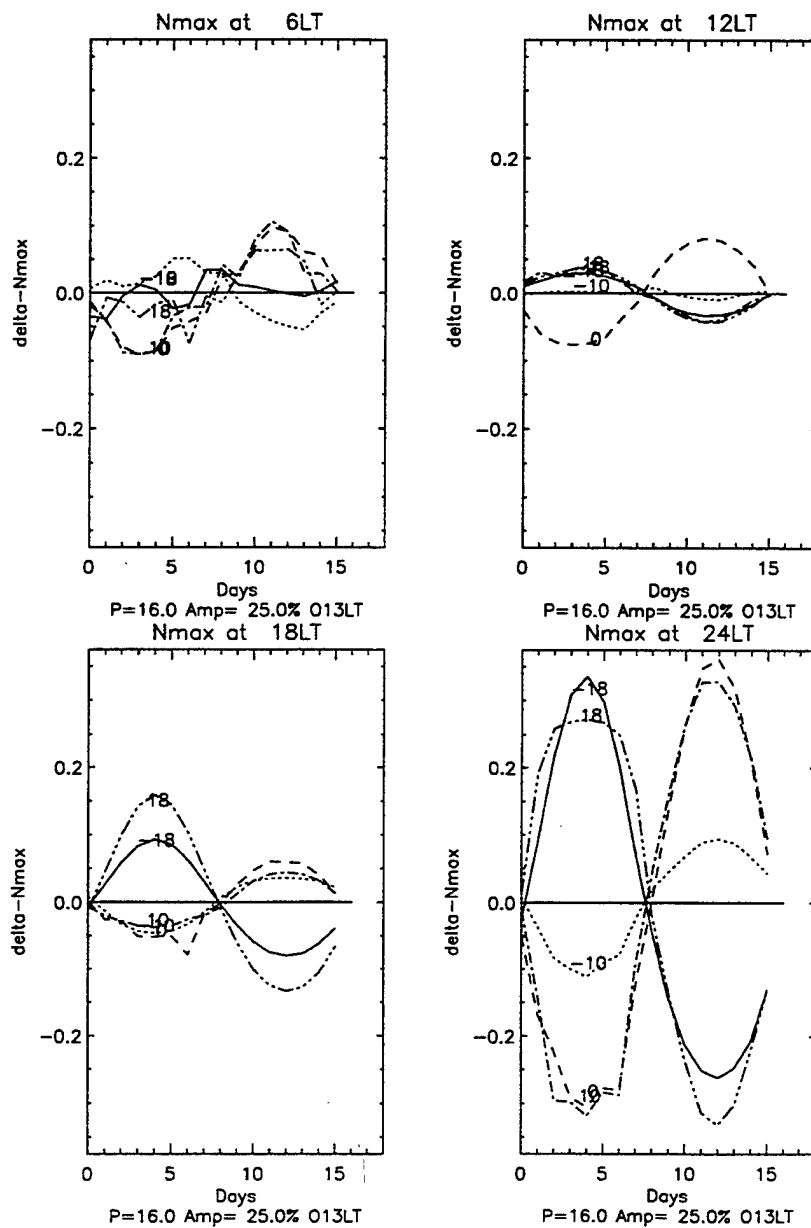


Figure 10. Wavelike ionospheric effects in the GTIM when a wavelike $\mathbf{E} \times \mathbf{B}$ disturbance is applied. This case was made for January, solar maximum, Huancayo sector conditions, using a 16-day wave and 50% peak-to-peak amplitude. The relative variation in Nmax at selected latitudes (18=solid line, -10=dotted, 0=dashed, +10=dot-dashed, +18=dot-dot-dot-dashed) is plotted as a function of the day during the period.

Overall, the model appears to give a good qualitative description of 16-day periodicities in foF2, if one creates a wavelike disturbance in vertical drift fields. Quantitatively, the modeled variations are typically somewhat smaller than those observed. Better quantitative agreement could be achieved by using vertical drifts in the model that were obtained from actual measurements, in order to better describe the quiescent conditions.

5 Applications Studies

Parallel to the development and refinement of theoretical ionospheric models is the ongoing development of applications-oriented models and empirical morphological descriptions of ionospheric phenomena and their terrestrial impact. Studies of this latter type are addressing particular needs of users of real-time or monitoring systems. Several studies of this type are described in the following section.

5.1 Ionospheric Ray-Tracing

A simple profile model was recently developed (Fox, 1994) where the profiles derived in a theoretical model at low latitudes were parametrized in terms of Chapman functions for each of the topside and bottomside; Chapman representations in this context are not so much physical descriptions as convenient mathematical descriptions of a basic ionospheric layer shape. This profile model differs in two important ways (1) the scale heights of the topside and bottomside layers are allowed to be height-dependent (2) the profile fit is obtained from a fit to both peak parameters and an additional control parameter, such as slab thickness or TEC. The model can thus provide climatological profile estimates, as well being able to accommodate additional real-time measurements.

The task undertaken here was to adapt this profile model for raytracing applications. The general problem in radiowave propagation is to be able to predict how various frequencies of waves will propagate for a given circuit under given conditions. Systems

already exist that can provide estimates based on climatology but it will not be clear in the field how any additional (real-time) observations may be used to help. The model described above is thus potentially very useful.

In the first instance, we used the model to provide climatological profiles for a number of locations along a designated circuit, and used a two-dimensional ray-tracing model to define the (zeroth order) propagation. Note that in this profile model both the electron density profiles and their first derivatives are analytic. Next, over the array of frequencies considered, the elevation angle required to reach the receiver from the transmitter is determined. Plots of elevation angle versus frequency are used as the basis for comparisons. Next, a ground truth ionosphere was set up for the same conditions, and the profile model given different amounts of information (peak or topside information, at various sets of locations) to update the specification and to ray-trace. What is being tested here is the ability of the Semi-empirical Improved Middle Plus Low-latitude Ionosphere (hereafter, SIMPLI) model to assimilate a small amount of data about the circuit and to successfully update radiowave propagation predictions accordingly. The means of testing is to compare the elevation angle loci of different ionospheres where each has resulted from a SIMPLI description using different amounts of “real” (in this case, from the Bent [1973] model) data. Imagine first only the Nmax value at the circuit midpoint is known; different methods of updating the description of profile parameters along the raypath were tested. Successively, the same tests were performed when other parameters (Hmax and slab thickness) and/or specified at other locations (along the circuit) are known. This determined how much data is required for the SIMPLI ray-tracing model to adequately revise its propagation predictions.

We illustrate typical results with the circuit Tx=(30,30), Rx=(20,20), June, F10.7=150, 1200UT, presented in Figure 11. The solid line is the initial guess from SIMPLI

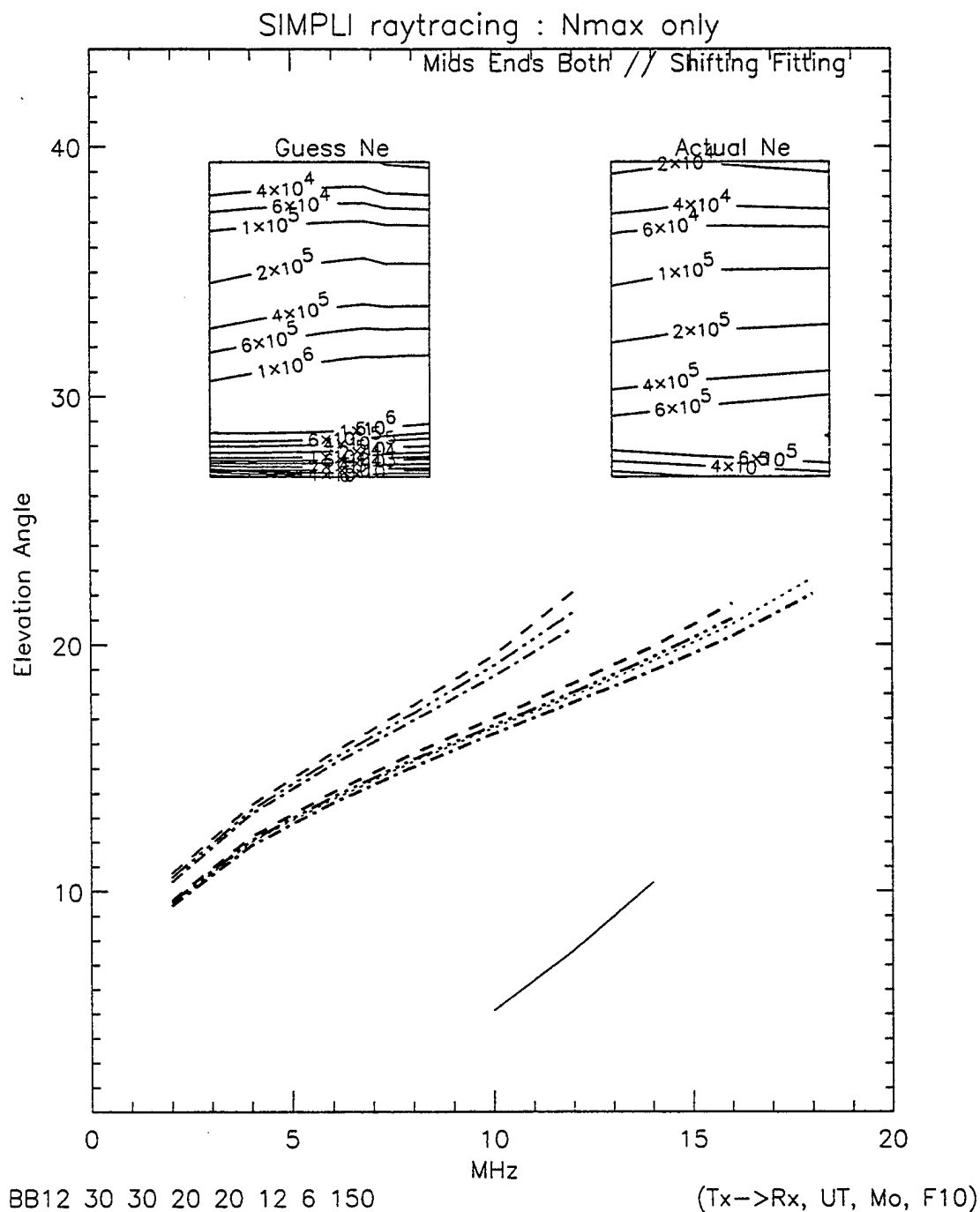


Figure 11. A demonstration of the abilities of the SIMPLI profile model in radiowave propagation predictions. Here, the solid line indicates the elevation angle versus transmission frequency for a given circuit obtained from climatological estimates (electron density contours in the left insert). The dotted line shows the same predictions made from the "ground-truth" ionosphere, shown in the right insert. The three topmost lines show the results when Nmax is updated at the circuit mid-point, end-points, and both, and when SIMPLI parameters along the path are shifted only the zeroeth order. The three lines lying nearest to the dotted line correspond to Nmax being refit along the whole path.

for the locus of elevation angle versus frequency for the circuit, based on the ionosphere seen in the left contour plot included in the figure. The dashed line is the locus from the “actual” ionosphere (from the Bent model), seen in the right contour plot, and clearly very different to the SIMPLI climatology in this case. Note both the different elevation angles in the true case, as well as the greater range of usable frequencies. It is important to be able to track changes of this nature. Also seen in this figure are two sets of three different lines, where the thinner lines are derived from one method of updating profile parameters, and the thicker lines from another, and where the data used is N_{\max} from the midpoint (dashed), ends of the circuit (dot-dashed) and all of the above (dot-dot-dot-dashed). In this case, the “fitting” method is seen to give a fairly good update for the ray propagation, even when only N_{\max} at the midpoint is known.

This same type of test was performed over a variety of one-hop circuits over a variety of conditions. In general, the fitting technique provided the more reliable means of updating the SIMPLI model for ray-tracing applications and overall, good results can be achieved when only N_{\max} at the circuit midpoint is available as an update. N_{\max} available at either the transmitter or receiver location also provides sufficient information to substantially improve propagation predictions.

5.2 Sensing the F region from DMSP

Earlier work performed at Boston University established a means of inferring N_{\max} and H_{\max} values from (GTIM modeled) observations of nightglow intensities (of the type to be measured by the Special Sensor Ultraviolet Spectroscopic Imager, or SSUSI). Here, a further study has been made, involving the use of these N_{\max} and H_{\max} estimates in conjunction with direct measurements of the in situ electron density from the Special Sensor for Ion, Electron and Scintillation Densities (SSIES). The specific task tackled was to derive a means of combining the in situ and peak ionospheric parameters into a specification of

the entire profile (or the total electron content, or TEC), performing data fusion on the ionospheric inputs from different sensors.

The method adopted is briefly as follows and is based on the profile model described in the previous section of this report. Chapman-like layers of altitude-dependent scale heights are anchored to the peak parameters. Initial estimates of the scale heights are obtained from a parametrization of results from the GTIM. The resultant in situ (840 km) density is compared to the SSIES value, and the difference is used to alter the internal scale heights, until a converged profile solution is obtained. In this fashion, smoothly-varying profiles are derived that are anchored exactly at the peak and to a predetermined precision in the topside. Estimates of TEC made thusly should be reliable because the profile will always asymptote to zero at high altitudes. It should also be noted that although the profile model is based on there being one topside "layer", it is not limited to applications where only one ionic species is present. The ability to adjust the effective scale height compensates for the transition from O^+ to H^+ .

Documentation has been prepared for this procedure and has been delivered to the Applied Physics Laboratory of Johns Hopkins University, in Laurel, MD.

5.3 Scintillations

A review was prepared on the scintillation activity reported in the literature at GPS frequencies, including observations at 1.2 GHz to 7 GHz with the appropriate scaling for the higher frequencies. It also included available data from GPS scintillation measurements. A first summary of available data was given at the Institute of Navigation-GPS Meeting in Salt Lake City in the Spring of 1995; this report has been published in the Proceedings of the Institute.

The most severe scintillation occurs in the equatorial anomaly region. In this region, during the solar maximum periods, amplitude scintillations at 1.5 GHz may exceed 20 dB

for several hours after sunset. Ascension Island in the Atlantic, Diego Garcia in the Indian Ocean, Hong Kong and Taiwan in the Pacific are some of the stations that fall directly under the anomaly region. However, areas within a few degrees of the magnetic equator may show only 5-7 dB fades. The occurrence of scintillation in the equatorial region is also a function of longitude.

The other potentially active regions are at auroral and polar cap latitudes. In the central polar cap in years of solar maximum, GPS receivers may suffer >10 dB fades. During magnetic storms auroral latitude reception may experience scintillation at a level to produce loss of lock. Models of scintillation occurrence exist and they are of use for planning purposes. However, the day-to-day variations of ionospheric parameters make short term forecasting difficult.

GPS satellites offer a unique source for measurements of amplitude and phase scintillation on a global scale. One receiver can record scintillation magnitudes and spectra at multiple propagation paths in the overhead sky. The data can be used to study ionospheric plasma structures, develop weather models of scintillation and can be scaled in frequency to support many operational systems. In turn, real time observations could allow for warning of fading problems since a large portion of the sky would be covered in the reception of signals from the multitude of satellites in the system. An approach to a warning system has been developed. Any interpretation of the fading structure and scintillation spectra must take into account both the ionospheric motion and the velocity of the satellite. For GPS receivers in aircraft, the motion of the heading of the aircraft also needs to be considered. With the use of more data and an understanding of the behavior of equatorial irregularities, techniques could be used to minimize the problem.

6 Meridional Wave Structures

SETA density measurements (normalized to a nominal altitude of 200 km) were analyzed to delineate characteristics of relatively small-scale waves (horizontal structures of order 150 to 2500 km) in the data. (Note: This analysis is restricted to *in-track* (latitudinal) structures; the analysis of longitudinal structures is addressed further below.) The spectral analyses were applied to all available orbits (approximately 15 to 18 per day) during 6 days in 1983 and 10 days in 1982, covering a range of geomagnetic conditions.

The complete results of this project appear in Forbes et al. (1995). A brief summary of results is presented below, and descriptions of the equations and algorithms (with samples of results) used in the analysis are provided in the following sections.

6.1 Summary of Results

As a result of this analysis, the lower thermosphere is found to be frequently characterized by wavelike structures corresponding to peak-to-peak density variations of order 10–40%. Orbit by orbit spectral analyses of densities normalized to 200 km altitude were performed, and these are combined together to construct average periodograms for magnetically quiet and active periods. Integration of these curves provides the relative percentage of total density variance attributable to various horizontal scales; for instance, 10% for $\lambda_H < 750$ km and 70% for $1500 < \lambda_H < 2500$ km. As geomagnetic activity increases from quiet ($K_p < 2$) to active ($K_p > 4$) levels, the spectral energy increases by a factor of two for wavelengths in the range 150 - 500 km and by a factor of four at longer wavelengths (1000 – 2500 km). In part the spectral energy enhancement at the longer wavelengths reflects mesoscale density variations unrelated to wave activity, but “direct” waves generated by auroral activity and which are known to travel long distances probably also make important contributions at these wavelengths. Similarly, a comparison of day vs. night periodograms for all orbits during 1983 was performed, illustrating the

enhancement in wave activity which occurs at scales shorter than 400 km during the night, whereas the spectral densities at wavelengths longer than 500 km are virtually the same. The magnetic activity enhancement at shorter scales is also significant, especially at low latitudes, since waves with these horizontal wavelengths are not expected on theoretical grounds to propagate very far within the thermosphere away from an auroral source. Moreover, the shorter scale waves regularly occur during geomagnetically quiet times when an auroral source mechanism is unlikely.

Much of our efforts were devoted to developing and applying various spectral methods to the data set. The following describes the methods of analysis which were developed, and presents sample results from the analysis which are alluded to in the above summary.

6.2 Method of Spectral Analysis

Standard periodogram spectral analyses were applied to each orbit of uninterrupted data. The orbits were categorized into three levels of magnetic activity in order to determine the dependence of periodicities on the magnetic activity. The categories are (a) quiet: $K_p \leq 2$; (b) average: $2 < K_p \leq 4$; (c) active: $K_p > 4$. In this section, we describe the results of periodogram spectral analysis performed on the density data.

The periodogram spectral analysis is based on estimating the distribution in frequency of the power $P_x(w)$ or the *power spectral density* (PSD) of a random signal $x[n]$ (density measurements in this analysis). This quantity can be shown to be related to the squared magnitude of the Fourier transform of the signal $x[n]$ by an extension of the Wiener-Khinchin theorem as follows:

$$P_x(w) = \lim_{M \rightarrow \infty} E \left[\frac{1}{2M+1} \left| \sum_{n=-M}^M x[n] e^{-jwn} \right|^2 \right]$$

where $E[\cdot]$ denotes the expectation operator. Neglecting the expectation operator, the PSD of the signal $x[n]$ of length N may be estimated as:

$$\hat{P}_x(w) = \frac{1}{N} \left| \sum_{n=0}^{N-1} x[n] e^{-jwn} \right|^2$$

which is the squared magnitude of the Fourier transform of $x[n]$ and can be evaluated using the FFT algorithm.

PSD's were generated for each uninterrupted orbit in the data base using 4096-point FFT's. Since each orbit of the satellite takes approximately 90 minutes, 1296 data points were analysed for each orbit in the case of the 1983 measurements.

6.3 Periodogram Averaging

The power spectra can be estimated more "reliably" by attempting to approximate the expectation operator described in the previous section. The technique is known as periodogram averaging and it is described in the following.

Suppose that $\hat{x}_1[n], \hat{x}_2[n], \dots, \hat{x}_K[n]$ are K uncorrelated instances (data records) of the same random signal $x[n]$. The *averaged periodogram* is then defined as: $\hat{P}_{avg}(w) = \frac{1}{K} \sum_{m=1}^K \hat{P}_m(w)$

where \hat{P}_m is the m^{th} periodogram given by: $\hat{P}_m(w) = \frac{1}{N} \left| \sum_{n=0}^{N-1} \hat{x}_m[n] e^{-jwn} \right|^2$

which is the squared magnitude of the Fourier transform of the m^{th} data record $\hat{x}_m[n]$. The variance of the averaged periodogram can be shown to be decreased by a factor of K while its expected value remains the same as the true PSD. In this sense the averaged periodogram is a more reliable estimate of the power spectrum.

Our averaged periodogram analyses are twofold. First, the average of the spectra for all of the uninterrupted orbits in each day is calculated. Second, the orbits are categorized into three levels of magnetic activity as described in the previous section, and for each level of magnetic activity an averaged periodogram is calculated.

The averaged periodogram corresponding to quiet and active orbits during the six days in 1983 are illustrated in Figure 12. This illustrates the enhancement in wave activity, especially at wavelengths longer than 1,000 km, which is generated in conjunction with magnetic disturbances.

Similarly, a comparison of day vs. night periodograms for all orbits during 1983 are illustrated in Figure 13. This plot illustrates the enhancement in wave activity which occurs at scales shorter than 400 km during the night, whereas the spectral densities at wavelengths longer than 500 km are virtually the same.

6.4 Wavelength Contribution to Signal Energy

In order to gain quantitative insight into the contribution of various wavelength ranges to the total signal energy, an equation known as Parseval's relation may be utilized, which relates a signal's total energy to its total spectral energy by:

$$\sum_{n=-\infty}^{\infty} |x[n]|^2 = \frac{1}{2\pi} \int_{2\pi} |X(w)|^2 dw$$

where $x[n]$ is the discrete-time signal corresponding to the data values, and $X(w)$ is the spectrum of the signal. The quantity on the left-hand side of the equation is the total energy in the time-domain signal $x[n]$, and $|X(w)|^2$ is referred to as the *energy-density spectrum*. The quantity of interest here, which we refer to as the "percentage contribution", is the ratio of the energy in an arbitrary wavelength range to the total signal energy.

According to Parseval's relation this quantity is proportional to the ratio of the energy in the arbitrary wavelength range to the total spectral energy. Since the wavelengths of interest here are all in the range of 0 to 2500 km, the "total" energy may be replaced by the energy in the range of 0 to 2500 km. The percentage contribution may therefore be defined as the ratio of the energy in an arbitrary wavelength range to the total energy of the signal with wavelengths between 0 and 2500 km. The averaged periodogram results described in the previous section are used to compute the percentage contribution for the density data during 1983 as a continuous measure of the ratio for all wavelengths in the range of 0 to 2500 km. The percentage contributions of the wavelengths are therefore both equal to 0% at 0 km and 100% at 2500 km, and increase continuously with increasing wavelength. As noted previously, integration of these curves provides the relative percentage of total density

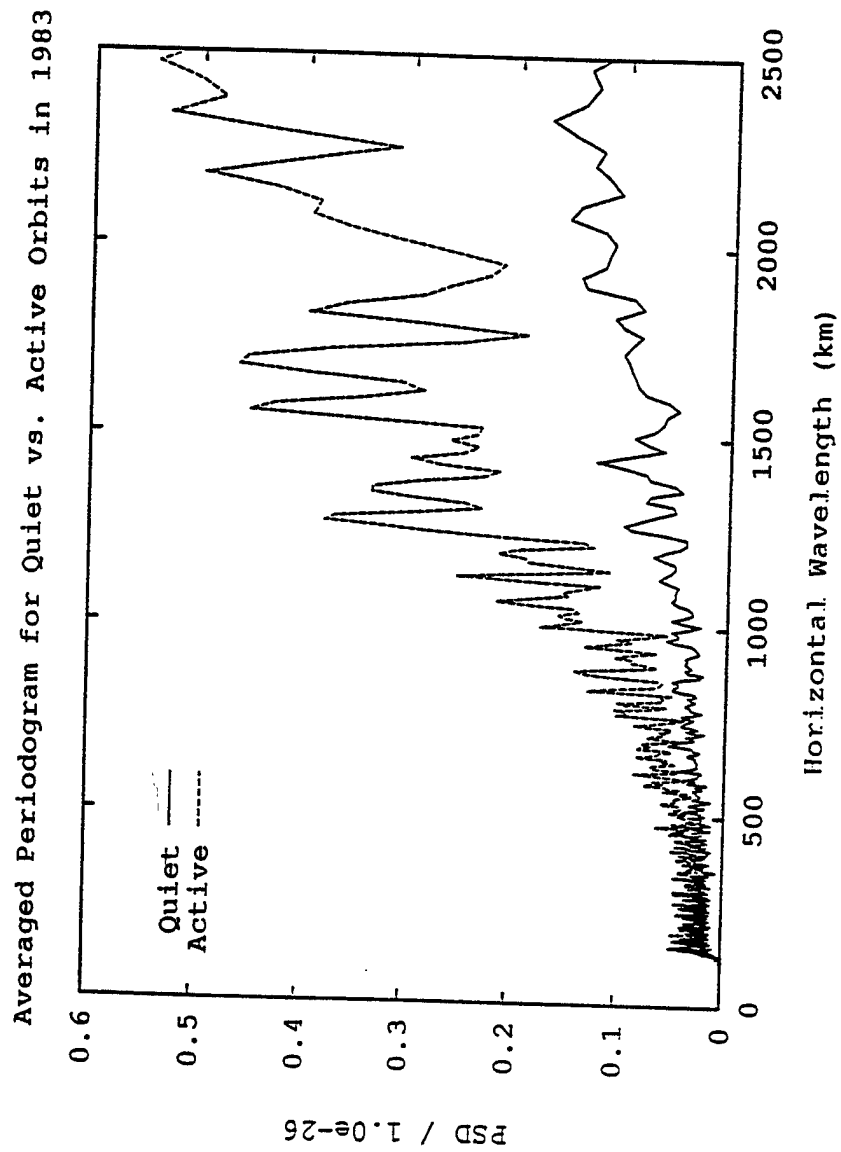


Figure 12. Averaged periodogram for quiet vs active orbits in 1983.

Day vs. Night Averaged Periodogram for 1983

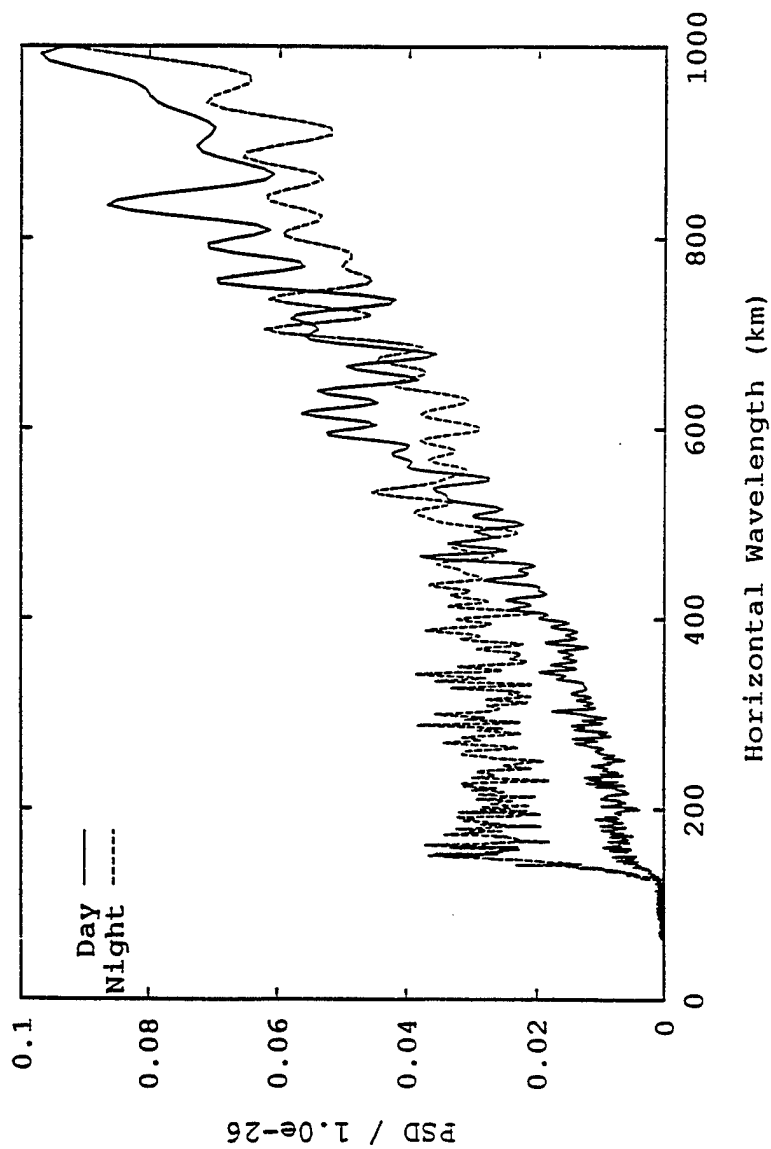


Figure 13. Day vs night averaged periodogram for 1983.

variance attributable to various horizontal scales; for instance, 10% for $\lambda_H < 750$ km and 70% for $1500 < \lambda_H < 2500$ km. As geomagnetic activity increases from quiet ($K_p < 2$) to active ($K_p > 4$) levels, the spectral energy increases by a factor of two for wavelengths in the range 150 - 500 km and by a factor of four at longer wavelengths (1000 - 2500 km).

The following conclusions may be drawn from the above work: **Meridional wave structures exist in thermospheric density with specific characteristics which depend on local time and magnetic activity. These variations are not included in empirical models. The majority of density variance associated with these waves occurs at scales in excess of 1,000 km, and therefore in principle their presence can be replicated in first-principles models of the thermosphere-ionosphere system.**

7 Magnetic Storm Perturbations

SETA-2 and SETA-3 data have been analyzed during the following periods containing significant changes in geomagnetic activity:

- (a) July 20-27, 1983
- (b) August 2-10, 1983
- (c) August 2-9, 1982
- (d) September 3-11, 1982
- (e) December 4-14, 1983

The results of this study are reported fully in Forbes et al. (1996). A summary of results is presented below, followed by sample results for two storm periods which are characteristic of the others studied.

7.1 Summary of Results

Density measurements near 200 km from the SETA (Satellite Electrostatic Triaxial Accelerometer) experiment are used to delineate the temporal, seasonal-latitudinal and day vs. night dependences of the response to magnetic storm-related perturbations in high-latitude energetic inputs. Five periods of geomagnetic activity are analyzed, and yield consistent results which can be interpreted within the framework of recent thermosphere-ionosphere simulations. In response to a change in magnetic activity level from quiet ($K_P \approx 1-2$) to active ($K_P \approx 4-7$) conditions, an increase in daytime (1030 LT) density of order 50-70% occurs between 60 and 80° geographic latitude in the summer hemisphere, with about half the maximum response in the winter hemisphere. This difference is mainly due to different ionization/conductivity levels (and hence joule heating rates) between the hemispheres. Dayside penetration of the disturbance at about the 50% intensity level is realized at the equator, whereas in the winter hemisphere equatorward penetration is much weaker. These effects are connected with the prevailing solar-driven circulation; the net summer-to-winter meridional flow facilitates equatorward advection of the disturbance bulge in the summer hemisphere, but hinders advection in the winter hemisphere. In both hemispheres the daytime solar-driven diurnal circulation tends to oppose equatorward penetration to the same degree. However, on the nightside (2230 LT) penetration at nearly the 100% level of both summer and winter disturbance bulges are realized to within 20° of the geographic equator. This behavior is associated with the equatorward advection in both hemispheres consistent with the nighttime component of the solar-driven circulation. Comparisons with the MSISE90 model [Hedin, 1991] show it to capture the salient features of the daytime behavior, but exhibits little day/night asymmetry, in contrast to the experimental results.

7.2 Sample Result

Various data visualization tools have been developed to depict the temporal, day vs. night, and latitudinal/seasonal trends characterizing the response of thermospheric mass density to changes in high-latitude heating during magnetically active periods. Data between 170 and 240 km are normalized to a constant altitude of 200 km. Sliding 11-rev (about 16 hours) means are applied to the data to remove smaller-scale features, and to serve as a "trend" for delineation of the residual densities (see following section).

Kp variations for two of the study periods, July 20-27, 1983, and August 1-10, 1983, are depicted in Figure 14. Figure 15 illustrates the latitude-time variations in total mass density "trend" occurring during the July 1983 period. Note the much larger response occurring in the summer hemisphere; this is due in part to the enhanced Joule heating connected with the larger ionization levels characterizing the summer ionosphere. There is also the tendency for the density perturbation to be carried from summer to winter due to the prevailing thermospheric circulation in that direction. The combination of these two effects gives rise to the large seasonal asymmetry in the density response depicted in Figure 15.

Figure 16 illustrates the SETA density response in the nightside (2230 LST) for the July 1983 period. Note that the density response penetrates much more easily to the equatorial region; this is due to the enhanced equatorward winds which characterize the nighttime thermosphere as opposed to the daytime thermosphere. The corresponding figure for MSISE90 (not shown) does not reflect this behavior, pointing to a shortcoming of this empirical model.

The following conclusions may be drawn: **The response of thermospheric density to magnetic activity is characterized by dependences on local time and season which may be interpreted in terms of prevailing (solar-driven) circulation**

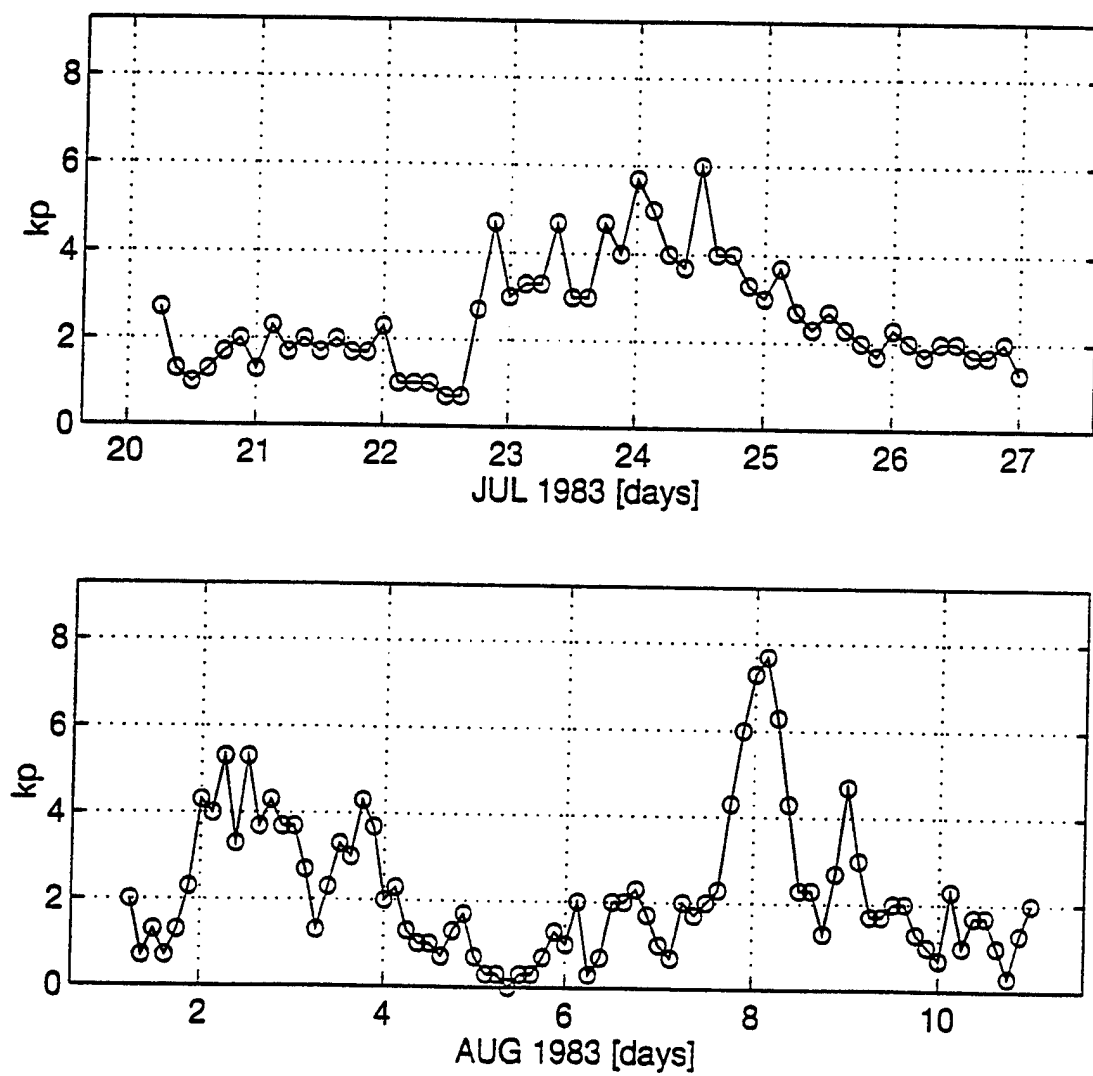


Figure 14. Kp variations for the July , 1983, and August, 1983 study periods.

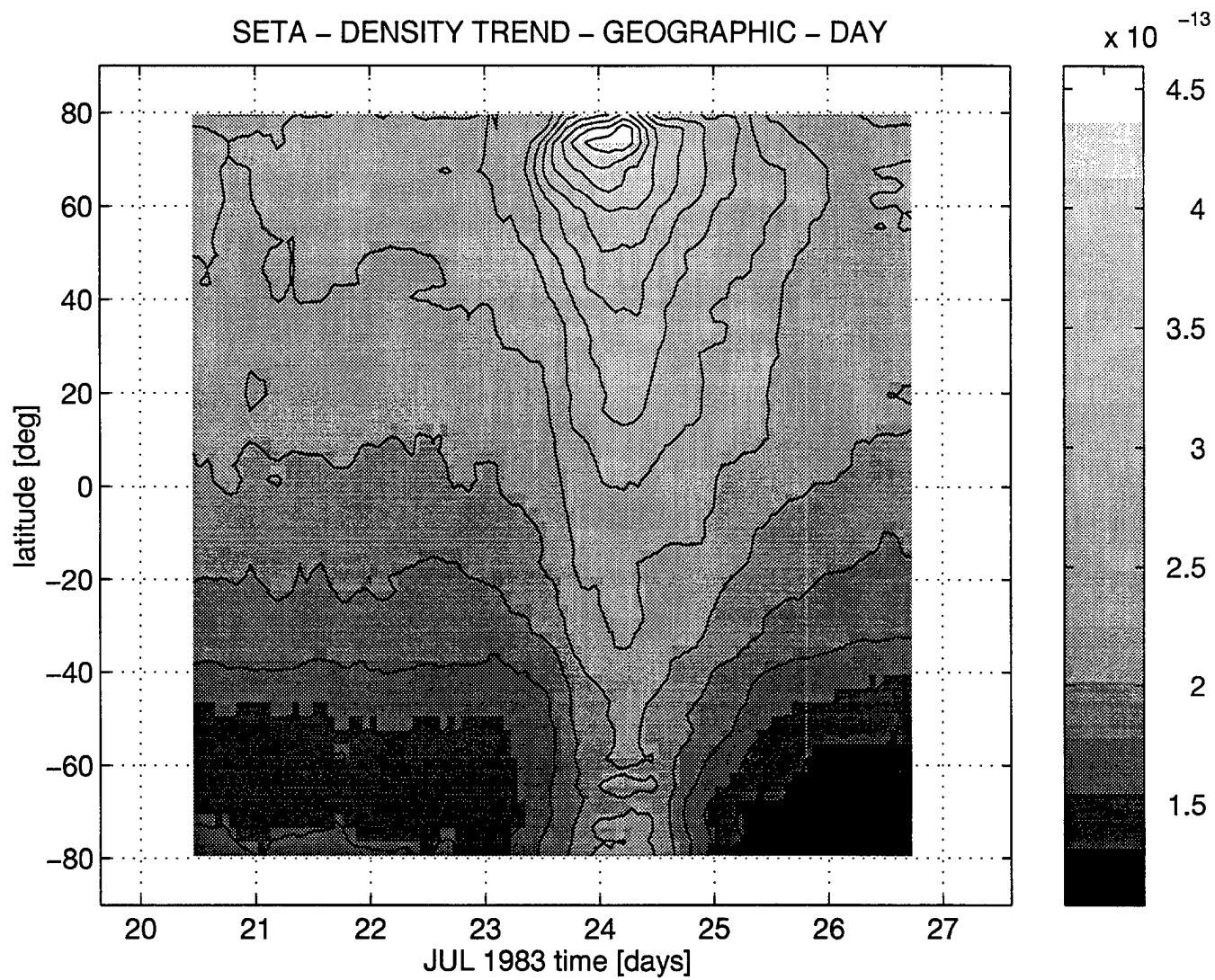


Figure 15. Daytime density variations during July 20-27, 1983.

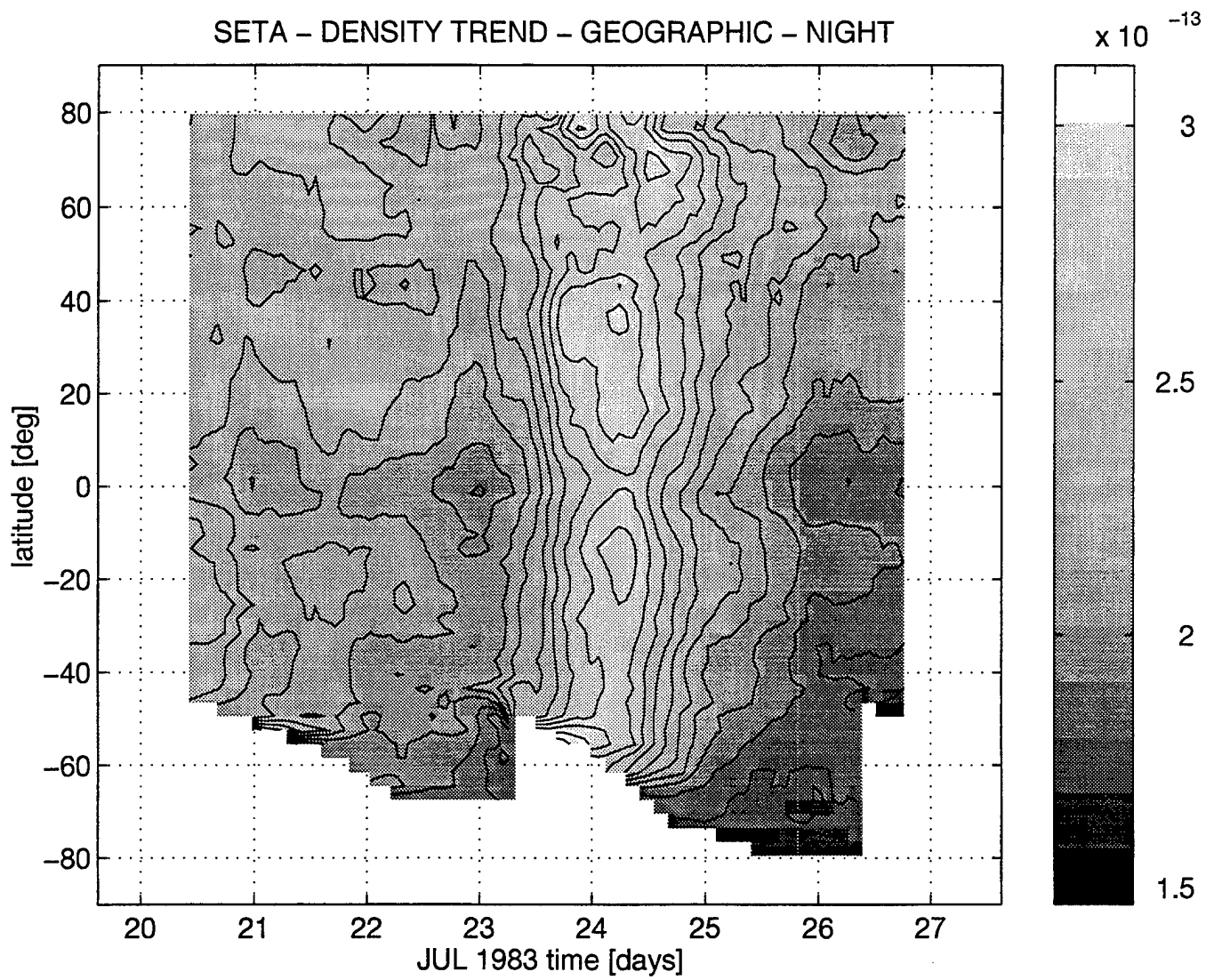


Figure 16. Same as Figure 15, except for nighttime.

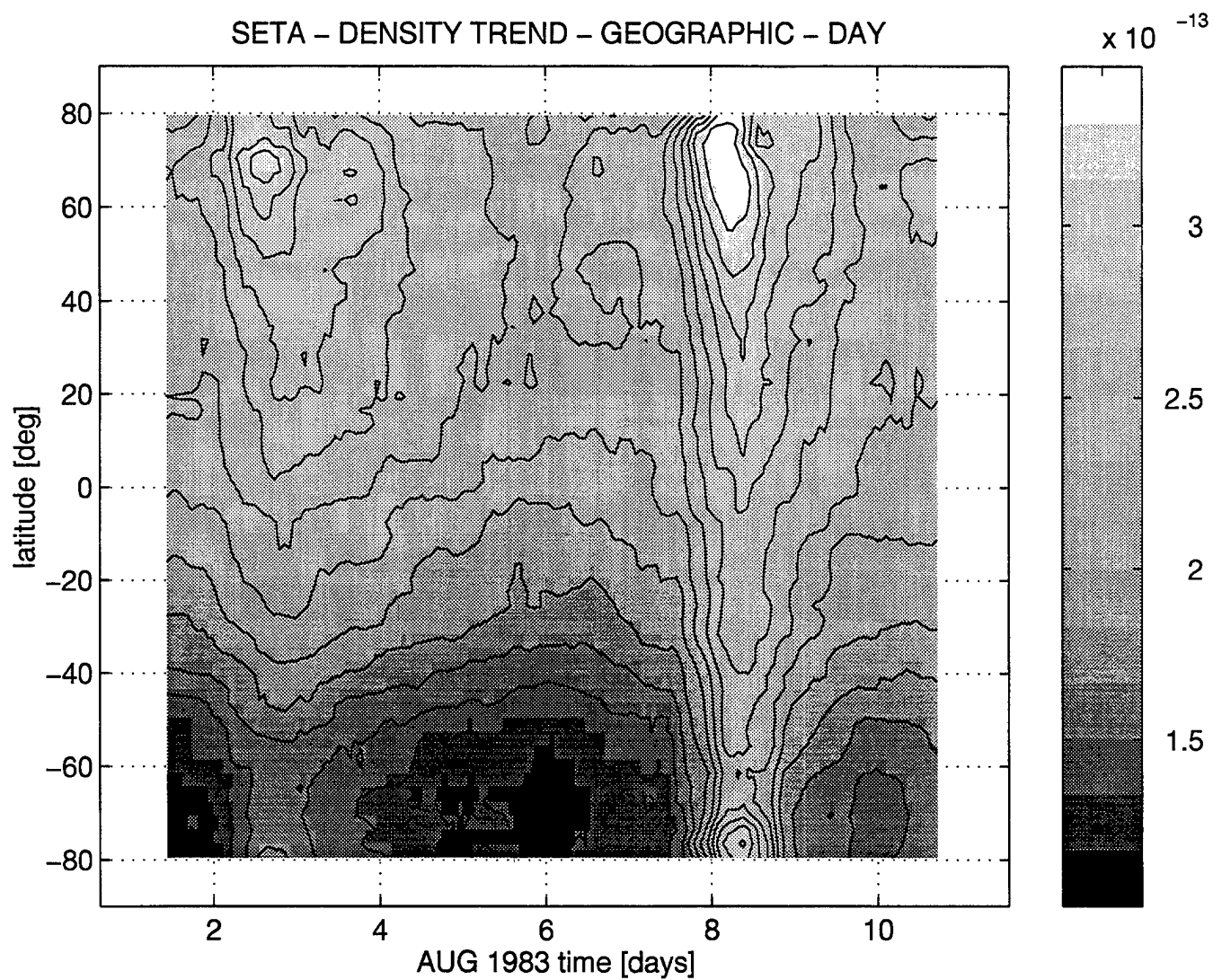


Figure 17. Same as Figure 15, except for August, 1983 study period.

systems. The data exhibit several characteristics which are not taken into account in existing empirical models. It is recommended that additional storms be analyzed to further solidify these results, and that empirical models used by the Air Force be updated accordingly.

8 Longitudinal Wave Structures

8.1 Longitude/UT Variation

The existence of a “longitude/UT” effect in the MSIS series of empirical models, which numerically describes the geomagnetic control of high-latitude thermospheric density, suggests that we examine the SETA data for such variations. Since the MSIS models suffer from sparse data coverage at low orbital altitudes and high solar activity, this comparison should be valuable in ascertaining the inadequacies of empirical models under these conditions. This comparison has been a major focus of this year’s contractual activities.

Figure 18 illustrates the time variation of SETA densities, normalized to 200 km and averaged between 20 and 40 degrees latitude, during July 21-26, 1983. MSIS90 density values were calculated for each SETA data point, and averaged in an identical fashion; these values are shown by the dotted line. Note that both the data and model exhibit a repeatable cycle with period of 24 hours or 360 degrees longitude; it is this variation which we refer to as the longitude/UT effect. Note that there is the appearance of the longitude/UT “amplitude” increasing with magnetic activity (a magnetic storm occurred on July 24).

For the present study, we primarily confine ourselves to the magnetically quiet periods during July 20-24, 1983, and December 4-10, 1983. All comparisons between MSIS and SETA correspond to SETA densities normalized to 200 km with the longitude/UT effect removed from the MSIS model. Variations in SETA data which we compare with MSISE90

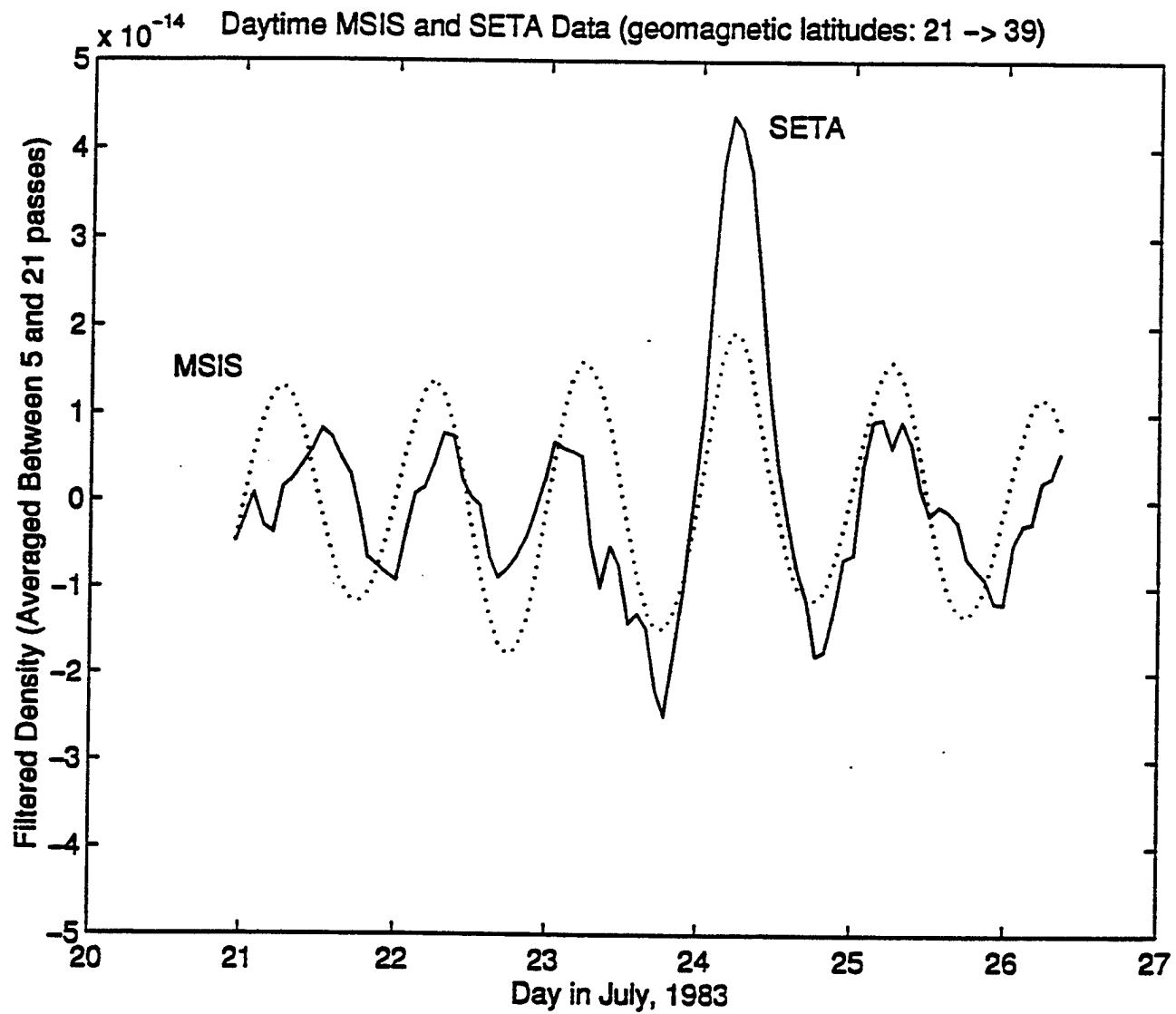


Figure 18. Comparison of SETA and MSISE90 density variations averaged over 20-20 degrees latitude at 1030 LT during July 20-26, 1983.

were extracted as follows. First, the long-term trend was established by performing a 17-orbit running mean. The residuals from this mean were then smoothed (5-orbit running mean) to remove the short-term variations. The result of this process is indicated in Figure 19 for dayside (1030 LT) data averaged over the 0-10° latitude range. The solid line in Figure 19 represents the least-squares fit of a sinusoid with a period of 24 hours (360° in longitude) to the SETA density residuals (circles). The dashed curve represents the corresponding MSISE90 prediction for this period. Note that the amplitude is given in terms of percent variation about the mean density. Figure 19 reveals a distinct periodicity in both the SETA data and MSIS which we are referring to here as the “longitude/UT” effect, although longitude and UT variations cannot be separated or distinguished from the sun-synchronous SETA orbit. The MSIS model exhibits a slightly smaller amplitude and a slight shift in phase with respect to the SETA density oscillation.

Figure 20 summarizes results from the above procedure for all available latitudes for the daytime data during this period. Amplitudes are calculated (a) taking into account the magnetically-active period, and (b) considering only the quiet days. The major model/data discrepancy to be gleaned from this plot is the significant latitudinal asymmetry depicted by the SETA data – a factor of 2 to 3 enhancement of the oscillation in the S. Hemisphere; on the other hand the MSIS model is symmetric about the equator.

An alternative form of depiction is presented in Figures 21 and 22. Here, we provide grey-scale plots of the density comparisons which also take into account the phase (i.e., longitude of maximum) of the “longitude/UT” oscillation. Only the magnetically undisturbed data are used in the fits. These plots also provide comparisons for the nighttime data for the July period, and daytime data for the December period. For the daytime data during July (left-hand panels in Figure 21), SETA and MSIS compare well in phase (i.e., longitude of maximum), but the SETA data suggest the phenomenon to

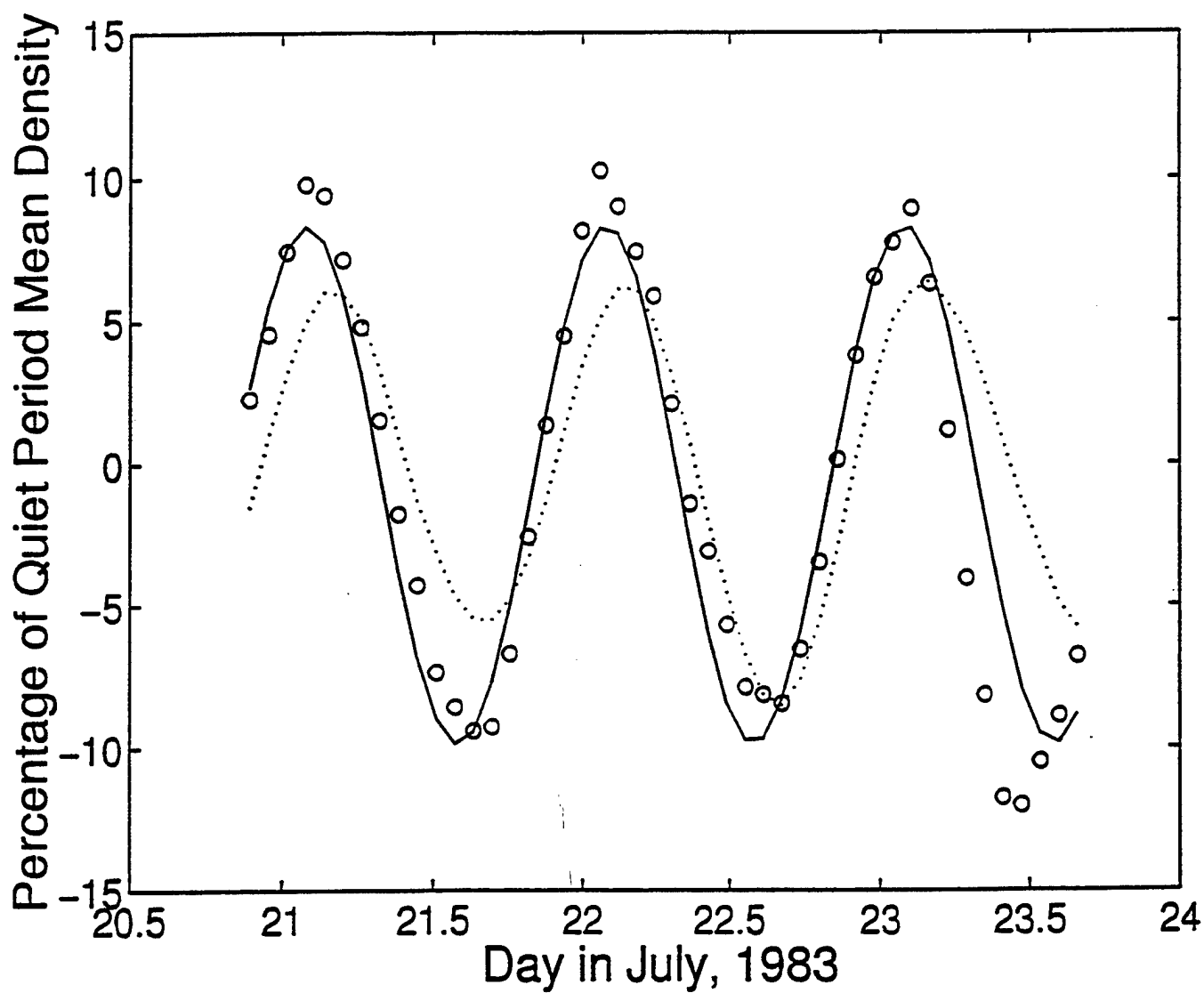


Figure 19. Comparison of "longitude/UT" variation in SETA densities (circles) with MSISE90 (dotted line) during the magnetically quiet period of July 21-23, 1983. Solid line represents least-squares fit of sinusoid to SETA data.

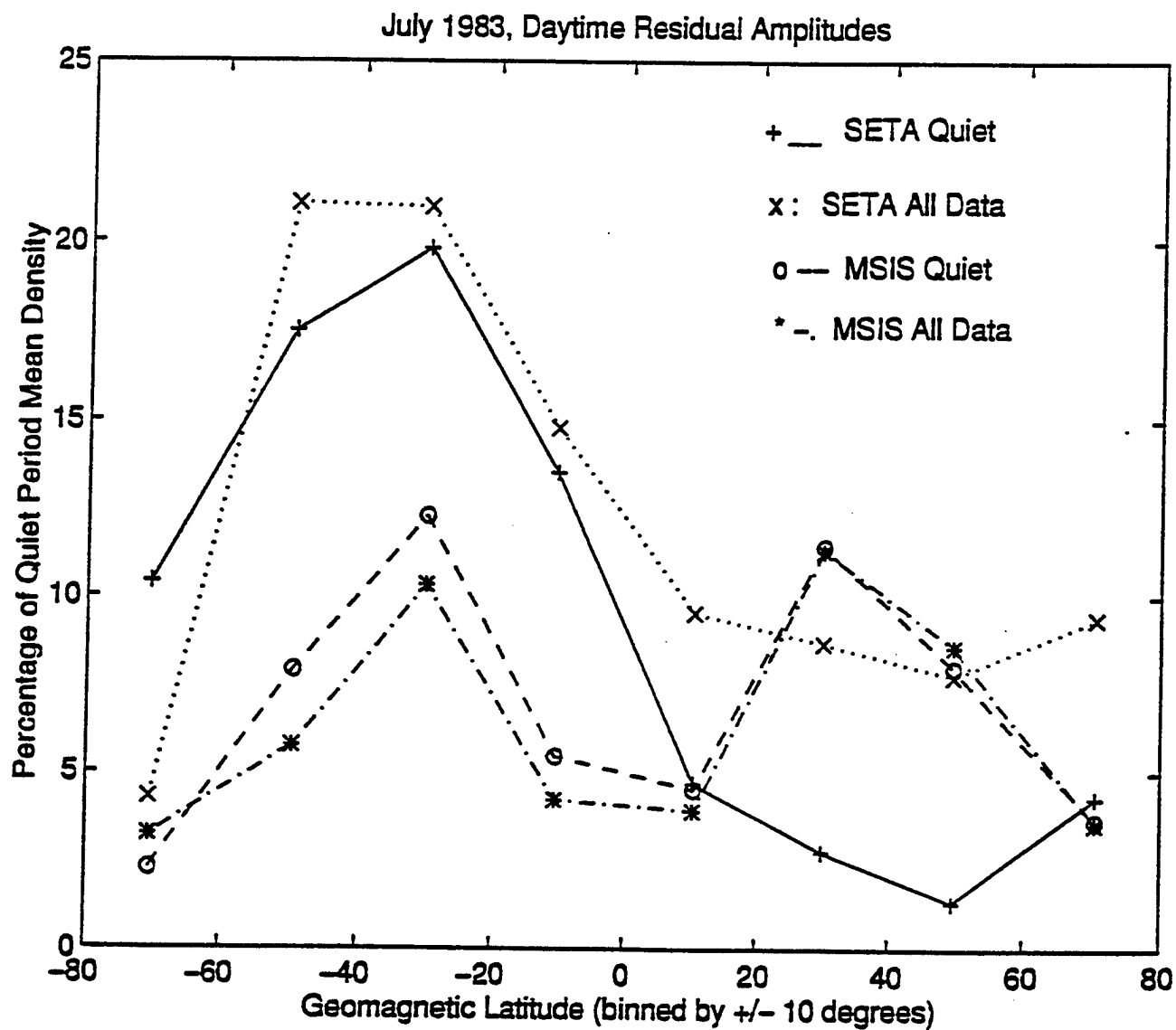


Figure 20. Comparison of amplitudes of "longitude/UT" variation between SETA and MSISE90 as a function of latitude, for daytime data during July 21-23, 1983.

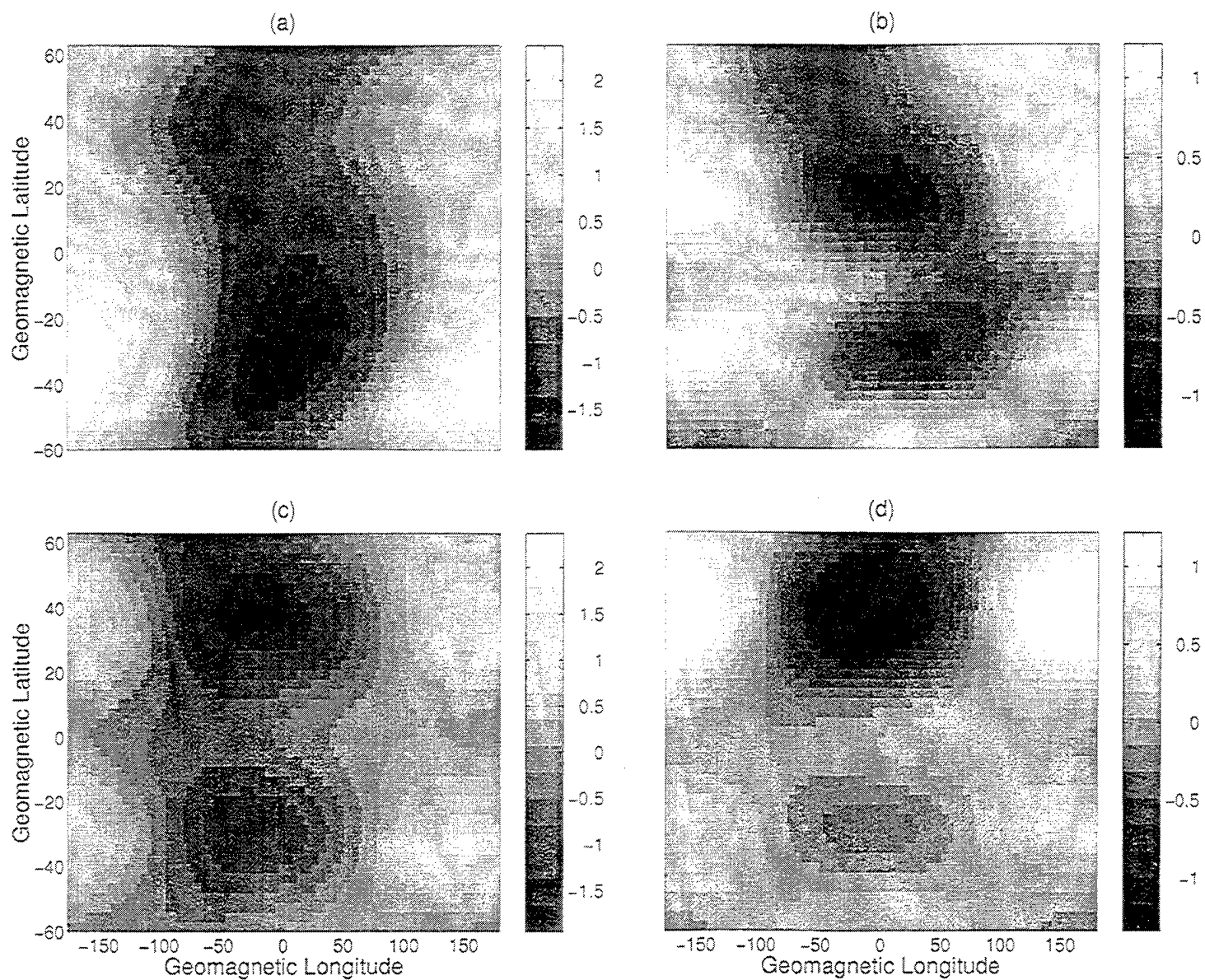


Figure 21. Longitude/UT dependence as revealed by Seta (top) and MSISE90 (bottom) total mass densities at 200 km during July 21-23, 1983. Left: daytime (≈ 1030 LT). Right: nighttime (≈ 2230 LT).

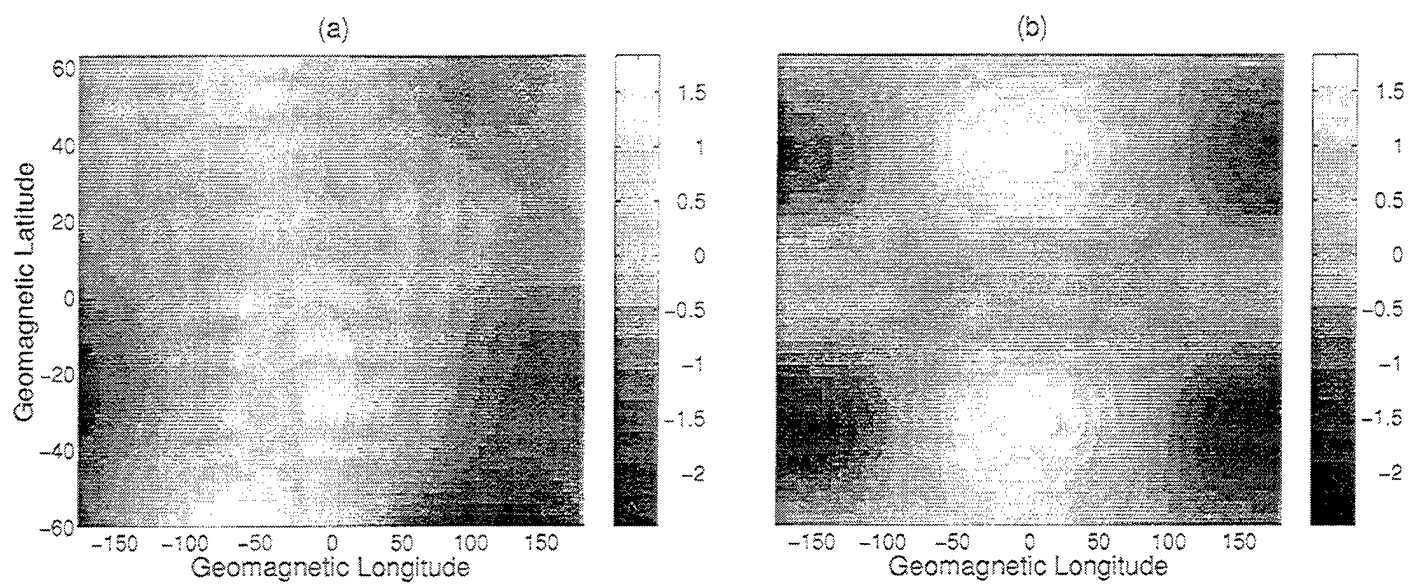


Figure 22. Longitude/UT dependence as revealed in SETA (left) and MSISE90 (right) daytime (≈ 1030 LT) total mass densities at 200 km during December 5-10, 1983.

be much more robust in the Southern Hemisphere as compared with MSIS. The right-hand panels illustrate the same results, except for nighttime (approx 2230 LT). Here, the converse is true: SETA is more symmetric about the equator, and MSIS is more asymmetric, with much larger perturbations in the Northern Hemisphere. Figure 21 illustrates similar comparisons for daytime data during December 1983, illustrating a very interesting 180 degree shift (for both MSIS and SETA) in the phase (longitude of maximum) of the phenomenon, as compared to the July period. Physical mechanisms underlying the above behaviors, including the seasonal phase shift, are not understood at the present time.

The main conclusion to be drawn from these comparisons is: **There exist significant seasonal/latitudinal differences, in amplitude and phase, between large-scale longitudinal structures revealed by SETA data in comparison to the MSISE90 model during magnetically undisturbed periods; these differences should be incorporated in future empirical modelling efforts in order to improve specifications of thermospheric density for various Air Force applications.**

8.2 Longitudinal Wave Structures

Given the above large-scale trends in the longitude structure of thermospheric density, subsequent efforts have focused on analysis and interpretation of the “residual density variations” superimposed on the large-scale structure. Samples of these residual structures for daytime data during July 20-24, 1983 and December 5-10, 1983, are provided in Figure 23. It is evident that there exist band-like structures extending in the north-south direction. The following describes our efforts to characterize these features quantitatively.

The main difficulty faced in analyzing and interpreting these features is with the space-time sampling inherent from a satellite. The SETA satellites are in sun-synchronous orbits, which means that local time is fixed and the satellite track is nearly at an angle of 90° with respect to the equator (actually, the angle is about 83°). The earth (and

atmosphere) is thus rotating below the satellite at an approximate rate of 360° longitude per day. Thus, time and longitude are varying continuously, and it is therefore difficult to separate longitude variations from time variations in the atmospheric density. This is especially the case when wave features may in principle be propagating eastward and/or westward with respect to the surface of the earth, as we well know that case to be in the troposphere and stratosphere. Spectral analysis of the data therefore leads to some ambiguity in interpretation. The difficulty may be summarized through the relationship given below

$$k_s = m \pm 1/T$$

where k_s is the zonal wavenumber viewed from the frame of the satellite, m and T are the earth-fixed zonal wavenumber (integer) and period (in days) for a particular oscillation, and the negative (positive) sign corresponds to westward (eastward) propagation. k_s need not be an integer. So, if k_s is found to be 1.33, for instance, from straightforward spectral analysis of the data, this could be interpreted as a westward-propagating $m=2$ oscillation with $T=1.5$ days, or an eastward traveling wave with $m=1$ and $T=3$ days. Other higher-order combinations are in theory possible, and often it is necessary to either live with the ambiguity, or to deduce the physically correct answer by imposing other constraints.

The most prominent value of k_s derived from spectral analyses of the SETA at different latitudes was a value of 4, with secondary peaks often occurring at 2, 3, 1, and 5. A superposition of spectra for the various latitude bands in the N. Hemisphere for the July daytime data (cf. Figure 23) is illustrated in Figure 24. For $k_s = 2$, for instance, we have as the lowest-order *mathematically* plausible waves $(m, T) = (0, 1/2), (2, \infty), (1, -1)$. The first corresponds to a zonally-symmetric semidiurnal tide; the second to a quasi-stationary (i.e., earth-fixed) wave of $s=2$; the third to an eastward propagating diurnal tide with $s=1$. We eliminate from consideration (m, T) since this represents a migrating diurnal tide

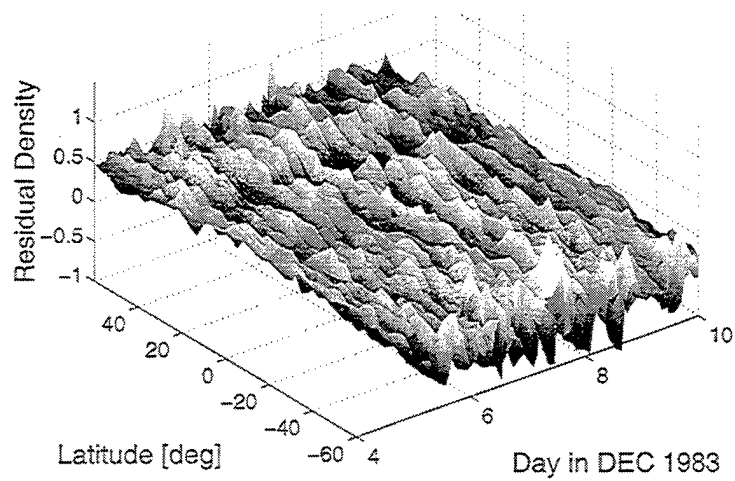
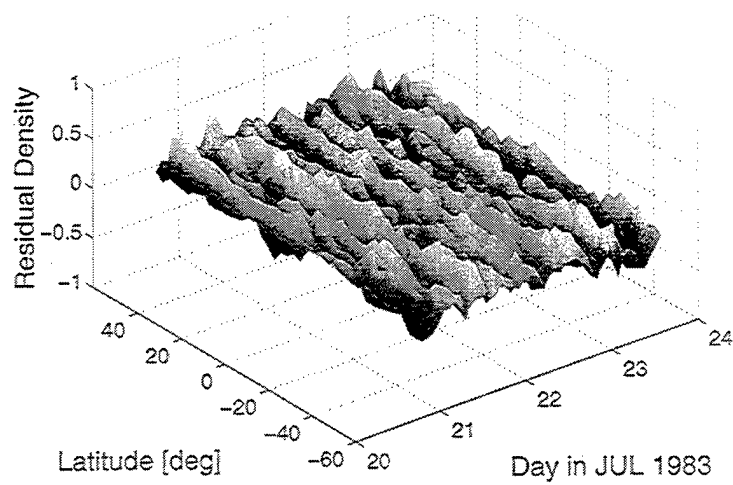


Figure 23. Density residuals as a function of latitude and time during magnetically quiet periods during July, 1983, and December, 1983.

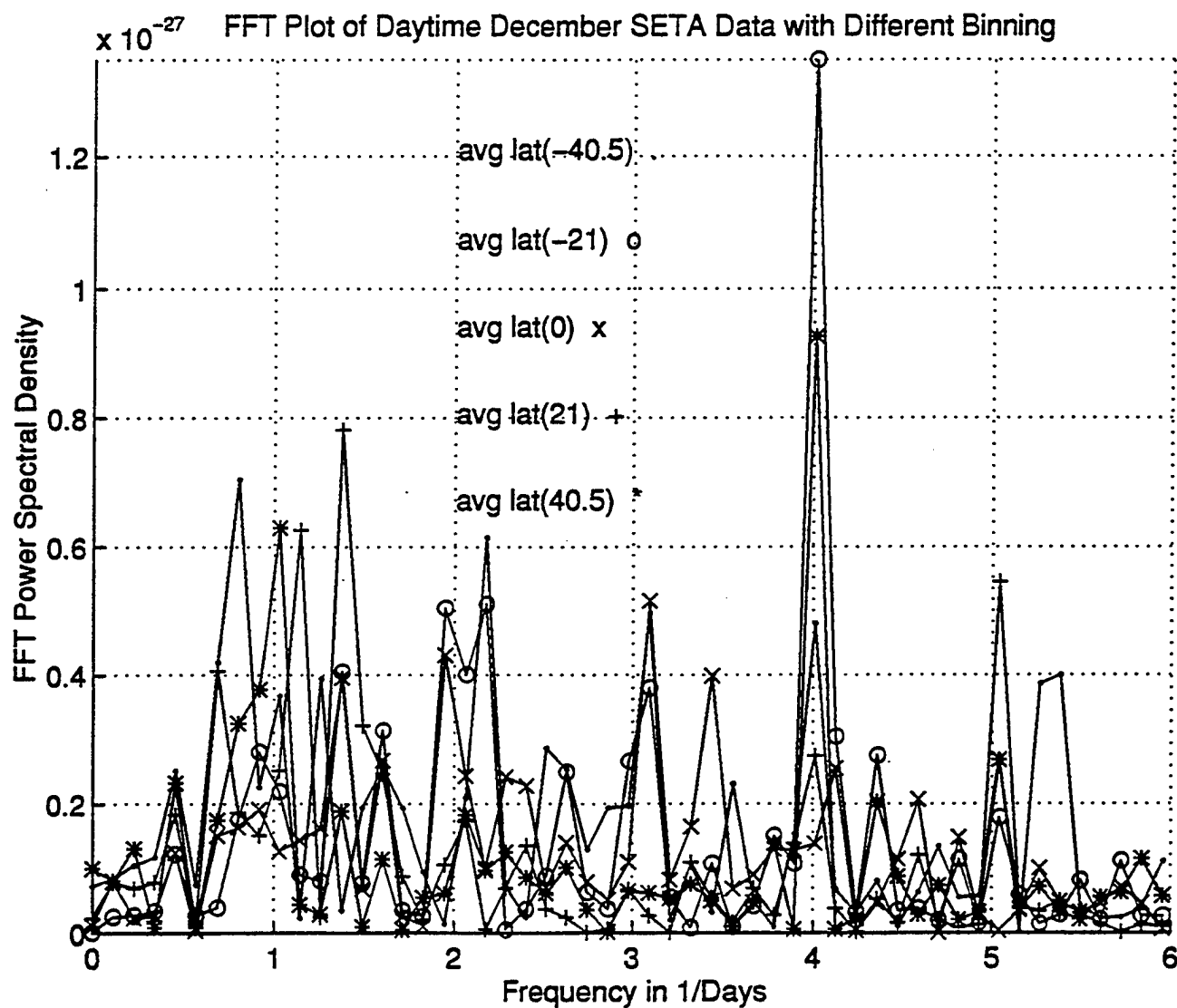


Figure 24. Superposition of spectra in different latitude bands, corresponding to the density residuals depicted in Figure 17 for July, 1983.

which cannot be detected from a single fixed-local time measurement (in other words, it does not meet the Nyquist criterion). The only plausible choice appears to be the quasi-stationary wave. For $k_s = 4$, we have $(m,T) = (4, \infty), (0, 1/4), (5,-1)$, etc. Again, the migrating semidiurnal tide $(2, 1/2)$ is eliminated from consideration, and there are no known reasons to expect an eastward-propagating wave or a zonally-symmetric 6-hour tide. Our tentative conclusion is that the structures seen in Figure 23, at least those consistent with apparent zonal wavenumbers of 4, 2, 3, 5, and 1 in Figure 24, correspond to earth-fixed features. It is noteworthy that the most prominent wavenumber, $s = 4$, also corresponds to the most prominent wavenumber in the decomposition of land-sea surfaces. This may suggest some relationship with lower-atmosphere physical processes. The thermospheric density amplitude variations associated with these features are about $\pm 2-4\%$.

We are led to the following conclusion: **Longitudinal wave structures of order $\pm 2-4\%$ exist in thermospheric density, with apparent earth-fixed zonal wavenumbers ranging between 1 and 5. Zonal wavenumber 4 appears to play an important role. Analyses of additional geophysical periods, perhaps using more sophisticated spectral analysis techniques, may lead to improved quantification and interpretation of this phenomenon.**

9 References

- Aarons, J. The longitudinal morphology of equatorial F-layer irregularities relevant to their occurrence, *Space Sci. Rev.*, **63**, 209, 1993.
- Anderson, D. N., A theoretical study of the ionospheric F-region equatorial anomaly, I. Theory, *Planet. Space Sci.*, **21**, 409, 1973.
- Banks, P. M. and G. Kockarts, *Aeronomy, Part B*, Academic Press, New York, 1973.
- Brace, L. H. and R. F. Theis, Global empirical models of ionospheric electron

temperature in the upper F-region and plasmasphere based on in situ measurements from the Atmospheric Explorer-C, ISIS 1 and ISIS 2 satellites, *J. Atmos. Terr. Phys.*, **43**, 1317, 1981.

Forbes, J. M. and S. Leveroni, Quasi 16-day oscillations in the ionosphere, *Geophys. Rev. Lett.*, **19**, 981, 1992.

Fox, M. W., A simple, convenient formalism for electron density profiles, *Radio Sci.*, **29**, 1473, 1994.

Forbes J. M. , F. A. Marcos, and F. Kamalabadi, Wave Structures in Lower Thermosphere Density from Satellite Electrostatic Triaxial Accelerometer (SETA) Measurements, *J. Geophys. Res.*, **100**, 14693, 1995.

Forbes J. M. , R. Gonzalez, F. A. Marcos, D. Revelle, and H. Parish, Magnetic Storm Response of Lower Thermosphere Density, *J. Geophys. Res.*, **101**, 2313, 1996.

Hedin, A. E., N. W. Spencer and T. L. Killeen, Empirical global model of upper thermosphere winds based on atmosphere and Dynamics Explorer satellite data, *J. Geophys. Res.*, **93**, 9959, 1988.

Hedin, A. E., M. A. Biondi, R. G. Burnside, G. Hernandez, R. M. Johnson, T. L. Killeen, C. Mazaudier, J. W. Meriwether, J. E. Salah, R. J. Sica, R. W. Smith, N. W. Spencer, V. B. Wickwar and T. S. Virdi, Revised global model of thermosphere winds using satellite and ground-based observations, *J. Geophys. Res.*, **96**, 7657, 1991.

Pi X. Q., M. Mendillo, P. Spalla and D. N. Anderson, Longitudinal effects of the ionospheric responses to substorms at middle and lower latitudes: A case study, *Ann. Geophys.*, **13**, 863, 1995.